

**Bioluminescent Calcium Indicator Protein and Gold Nanoparticle-enhanced
Bioluminescence**

A Thesis
Presented to
The Academic Faculty

By

Zuhui Wang

In Partial Fulfillment for the Degree
Master of Science in Bioengineering

Georgia Institute of Technology

May 2018

Copyright © 2018 by Zuhui Wang

**Bioluminescent Calcium Indicator Protein and Gold Nanoparticle-enhanced
Bioluminescence**

Approved by:

Dr. Robert E. Gross, Advisor
Department of Neurosurgery
Emory University

Dr. Lily S. Cheung
Department of Chemical and Biomolecular Engineering
Georgia Institute of Technology

Dr. Kostas Konstantinidis
School of Civil and Environmental Engineering
Georgia Institute of Technology

Date Approved: March 27, 2018

ACKNOWLEDGMENTS

I would first like to thank my thesis advisor Dr. Robert Gross for giving me the opportunity and resources of studying molecular biotechnology in his laboratory to complete my master's degree.

I would also like to thank Dr. Ken Berglund, Assistant Professor in the Dr. Gross's lab. Ken was my experimental teacher, who was always there for help. He consistently allowed this paper to be my own work and steered me in the right direction.

I would also like to give special thanks to my parents. Without your support, I could not be here.

TABLE OF CONTENTS

ACKNOWLEDGMENTS	iii
LIST OF TABLES	vi
LIST OF FIGURES	vii
LIST OF ABBREVIATIONS	ix
SUMMARY	x
Chapter 1 INTRODUCTION.....	1
1.1 Motivation.....	1
1.2 Research Objectives	3
Chapter 2 LITERATURE REVIEW	6
2.1 General Characteristics of Ca ²⁺ Indicator	6
2.1.1 Ca ²⁺ Affinities	7
2.1.2 Spectral Properties	10
2.1.3 Indicator Forms	11
2.2 Chemically Synthesized Ca ²⁺ Indicator	12
2.3 Genetically Encoded Ca ²⁺ Indicator	13
2.3.1 Ca ²⁺ binding protein motifs	13
2.3.2 FRET-based GECIs	15
2.3.3 Single fluorophore-based GECIs	19
2.4 Localized Surface Plasmon Resonance (LSPR)	21
2.5 Gold Nanoparticle (AuNP) and Protein Conjugation	23
2.5.1 AuNP size	24
2.5.2 Hydrophobicity	24
2.5.3 Surface chemistry.....	25
Chapter 3 Ultrasensitive Bioluminescent Calcium Indicator Protein	26
3.1 Introduction.....	26
3.2 Methodology	29
3.2.1 Plasmid Design	29
3.2.2 Bioluminescent Intracellular Ca ²⁺ Response in HEK293 Cells.....	30
3.2.3 Fluorescent Intracellular Ca ²⁺ Response in HEK293 Cells	32
3.3 Results and Discussion	34
3.3.1 Structure-based Design of the Ca ²⁺ Indicators.....	34
3.3.2 Intracellular Ca ²⁺ Response in HEK293 Cells.....	35
3.3.3 Evaluation of Performance	40

Chapter 4 Gold Nanoparticle Enhanced Bioluminescence	42
4.1 Introduction.....	42
4.1.1 Introduction of luminopsin	42
4.1.2 Ni-NTA-Au conjugation with histidine	43
4.2 Methodology	45
4.2.1 Plasmid Design	45
4.2.2 <i>In vitro</i> AuNP bioluminescence enhancement.....	46
4.3 Results and Discussion	48
4.3.1 Structure of his-tagged GLuc(LMO)	48
4.3.2 <i>In vitro</i> Ni-NTA-Au Bioluminescence Enhancement in HEK293 cells.....	48
4.3.3 Evaluation of the Performance.....	53
 Chapter 5 Conclusion of the Thesis	 55
 REFERENCES	 57

LIST OF TABLES

Table 1 High affinity chemically synthesized Ca^{2+} sensors	12
Table 2 Comparison of Biochemical Properties of Purified GCaMP series sensors...	20
Table 3 Biophysical properties of Ca^{2+} indicators in HEK293 Cells	39
Table 4 Primers Used in QuikChange	46

LIST OF FIGURES

Figure 2-1 Excitation spectrum of Fura-2 dye measured at emission wavelength of 510 nm with free Ca^{2+} from 0 – 39.8 μM .	11
Figure 2-2 Structure of typical EF-hands and its Ca^{2+} binding center.	14
Figure 2-3 Schematic of the Ca^{2+} coordination in a canonical EF-hand.	15
Figure 2-4 Dependency of FRET efficiency (E_{FRET}) on the distance (r) between a donor-acceptor pair with an assumed Förster radius R_0 of 50 Å.	16
Figure 2-5 Calmodulin (CaM)/FRET-based GECIs.	17
Figure 2-6 Circular permutation of GFPs.	19
Figure 2-7 Schematic representation of GCaMP and its crystal structure.	20
Figure 2-8 Schematic diagrams illustrating (A) a surface plasmon polariton (or propagating plasmon) and (B) a localized surface plasmon.	23
Figure 3-1 Schematic representation of sbGLuc and GCaMP6s based Ca^{2+} indicators and corresponding 2A negative control.	28
Figure 3-2 Schematic representation of the mechanism of “self-cleaving” 2A peptides.	29
Figure 3-3 Simplified amino acid sequences of GCaMPGLuc, GLucGCaMP and GCaMP2AGLuc. Specifically, 2A in GCaMP2AGLuc is T2A peptide.	30
Figure 3-4 Plate arrangement of transfection and free Ca^{2+} calibration.	31
Figure 3-5 Workflow of the image analysis.	33
Figure 3-6 Crystal structure of GCaMP6m from the top view	35
Figure 3-7 <i>In vitro</i> Ca^{2+} titration by BRET.	36
Figure 3-8 Donor-acceptor energy transfer.	37
Figure 3-9 <i>In vitro</i> Ca^{2+} titration by fluorescence.	38
Table 3 Biophysical properties of Ca^{2+} indicators in HEK293 Cells	39
Figure 3-10 Emission ratio of GCaMPGLuc and GLucGCaMP on two dates separated six months exhibits consistent response.	41
Figure 4-1 Schematic representation of Ni-NTA-Au binding with histidine and its structure.	43
Figure 4-2 Schematic representation of Ni-NTA-Au binding with Nhis_GLuc(LMO).	44

Figure 4-3 Schematic sequence structure of the original eLMO3 (GLuc(LMO)) and designed three his-tagged eLMO3.	45
Figure 4-4 Nhis_GLuc(LMO), NChis_GLuc(LMO), Chis_GLuc(LMO) and GLuc(LMO) expression in HEK293 cells..	49
Figure 4-5 Total light yield of the four GLuc(LMO)s..	49
Figure 4-6 Enhancement factor of Nhis_GLuc(LMO), NChis_GLuc(LMO), Chis_GLuc(LMO) and GLuc(LMO), after incubating with 0.5 nM of various size of AuNPs.	51
Figure 4-7 Enhancement factors of Nhis_GLuc(LMO), NChis_GLuc(LMO), Chis_GLuc(LMO) and GLuc(LMO) after incubating with 0.5, 1 and 5 nM of Ni-NTA-Au and simple Au (both d = 10 nm).....	53

LIST OF ABBREVIATIONS

AuNP: Gold nanoparticle,
BRET: Bioluminescence resonance energy transfer,
CaM: Calmodulin,
cpEGFP: Circularly permutated enhanced green fluorescent protein,
FRET: Förster resonance energy transfer,
GECI: Genetically encoded calcium indicator,
GLuc: *Gaussia* luciferase,
LMO: Luminopsin,
LSPR: Localized surface plasmon resonance,
sbGLuc: "Slow-burn" *Gaussia* luciferase",
SPR: Surface plasmon resonance,
TnC: Troponin C,
XFP: Fluorescent protein.

SUMMARY

Bioluminescent proteins have been extensively used as a light emission source for many fusion proteins and have a wide range of applications in imaging and cell signaling studies. In this study, the smallest known luciferase from the marine copepod, *Gaussia princeps*, was used to engineer novel bioluminescent sensors and novel methods to enhance bioluminescence intensity. In the First part of the study, two bioluminescent calcium sensors were developed, which were composed of a variant of *Gaussia* luciferase (sbGLuc) and the fluorescent calcium indicator protein, GCaMP6s. The two designs allowed bioluminescence resonance energy transfer (BRET) and they exhibited excellent dynamic range. In the Second part of the study, several strategies to enhance bioluminescence by conjugating sbGLuc with gold nanoparticles were carefully examined. On average, 26% enhancement on bioluminescence was achieved. The new sensors together with the gold nanoparticle-enhanced bioluminescence should be useful for various studies in various fields such as neuroscience and cell biology.

CHAPTER 1 INTRODUCTION

1.1 Motivation

Bioluminescence, which is luciferase-catalyzed light-emitting reactions of molecular oxygen with its substrate luciferin, provides a potent biomolecular toolbox to study cell biology. One promising application of bioluminescence is designing robust and sensitive biosensors to monitor and further manipulate various cell activities. In living cells, Ca^{2+} is a crucial signaling ion that is poised at the core of a sophisticated network of signaling pathways (Dodd, Kudla, & Sanders, 2010). These pathways integrate information from biotic and abiotic stimuli to intricately control gene expression. Intracellular Ca^{2+} is central to a multitude of physiological processes ranging from bone formation to muscle contraction to neuronal signaling and exocytosis (Berridge, 1993). Abnormal Ca^{2+} signaling transduction will lead to severe pathological consequences such as skin disorders, heart disease, skeletal muscle defects, neurodegeneration, disorders of the central nervous system (Carafoli, 2004). Thus, great interest arises to monitor intracellular Ca^{2+} concentration $[\text{Ca}^{2+}]$ in real time. Intracellular $[\text{Ca}^{2+}]$ takes the form of free Ca^{2+} , or more precisely, the activity of cytosolic free Ca^{2+} , $[\text{Ca}^{2+}]_i$. In neurons, $[\text{Ca}^{2+}]_i$ is maintained around 100 nM, variously reported as 20,000 to 100,000-fold lower than typical extracellular concentration so that Ca^{2+} can work as a critical intracellular signal in various processes.

All those characteristics of intracellular free Ca^{2+} require that live cell Ca^{2+} measurements possess ultra-sensitivity, stability and non-cytotoxicity. So far, fluorescence-based Ca^{2+} indicators are the only successful approach to track real-time intracellular Ca^{2+} in cellular processes (M. Mank & Griesbeck, 2008). Whether there are chemically synthesized fluorescence dye or genetically encoded Ca^{2+} indicators (GECIs), they work on the changes of the fluorescence signal, which requires external light to excite fluorophore. Such approaches require implantation of fiber optics for *in vivo* excitation, which may impair the results accuracy due to improper installation or even tissue damage. Long term monitoring and control also are challenging due to potential photobleaching of fluorophore and phototoxicity by using intensive excitation light. Thus, developing a robust sensitive genetically encoded Ca^{2+} indicator without the need of external excitation light is strongly desired, which could

be achieved through coupling traditional fluorescence based GECIs with bioluminescence.

Besides monitoring cell activities, bioluminescence can coordinate with other light-sensitive channel proteins (*e.g.* channelrhodopsins, proton or chloride pumps) to manipulate cell (especially neuron) activities, which further developed into optogenetics techniques. The efficiency of optogenetic probes heavily depend on spectral properties of luciferase, such as intensity, peak wavelength, kinetics, *etc.*

Compared with extensively studied firefly luciferase (FLuc) from *Photinus pyralis* and *Renilla* luciferase (RLuc) from *Renilla reniformis*, more recently discovered *Gaussia* luciferase (GLuc) from the marine copepod *Gaussia princeps* has been shown to give much brighter bioluminescence than either FLuc or RLuc (Goerke, Loening, Gambhir, & Swartz, 2008; Tannous, Kim, Fernandez, Weissleder, & Breakefield, 2005). However, native GLuc has burst kinetics with a half-life of around 1 min and still dim bioluminescence intensity, limiting the applications in long time scale detection (Aslan & Geddes, 2009; Karolin & Geddes, 2012). Welsh and Patel (2009) obtained a series of mutated GLuc by the point mutations of methionines to leucines, among which M43L and M110L mutation (named as “slow-burn” GLuc or sbGLuc) provided prolonged light emission with a half-life of around 14 min while preserving much of the bioluminescent intensity. Thus, if the bioluminescent intensity of sbGLuc is further enhanced with a simple strategy, it should be a useful approach to ameliorate the performance of bioluminescence based optogenetic probes, such as luminopsin. LMO3 luminopsin (luciferase + opsin) is an optogenetic probe based on the fusion protein of sbGLuc with *Volvox* channelrhodopsin 1 (VChR1) developed in our lab (Berglund et al., 2016). If the bioluminescence intensity of sbGLuc gets enhanced, VChR1 could be more activated to generate stronger depolarization upon application of the same amount of coelenterazine (CTZ), a substrate for GLuc. By coupling localized surface plasmon with excitation-state molecules via non-radioactive energy transfer (also known as localized surface plasmon resonance, LSPR), Au nanocrystals are demonstrated to enhance bioluminescence of horseradish peroxidase (HRP) nanoclusters (Du, 2014). Thus, LSPR provides a promising mechanism to achieve bioluminescence enhancement.

1.2 Research Objectives

The **overall objective** of this research was first to develop genetically encoded Ca^{2+} indicators (GECIs) that can operate by noninvasive bioluminescent excitation while preserving fluorescence excitability; and second to develop a novel bioluminescence enhancement strategy of coupling gold nanoparticles with sbGLuc. This research was performed through two specific aims as outlined below:

1. Evaluate the Ca^{2+} binding properties of proposed GECIs under bioluminescence excitation and fluorescence excitation separately in HEK293 cells.

Ca^{2+} affinity and dynamic range are crucial parameters when describing Ca^{2+} binding properties of a given GECI. The dissociation constant (K_d) describes how tightly an indicator binds Ca^{2+} ions, and apparent K_d is more frequently reported when the binding process is cooperative. Previous studies (Nakai, 2001) have shown that calmodulin cooperatively binds with Ca^{2+} ions, which can be depicted by the Hill equation. Therefore, we aimed to characterize the bioluminescence-fluorescence signal change of our GECIs under calibrated intracellular gradient of $[\text{Ca}^{2+}]$ in HEK293 cells. Subsequently, the regression of signal changes with the Hill equation can provide apparent K_d and Hill coefficient of each variant of GECIs. Together with the dynamic range of signal changes, we can systematically evaluate the performance of our new GECIs under bioluminescence and fluorescence working conditions, which lays the foundations for future *in vivo* applications.

2. Provide experimental evidence of proposed GECIs working mechanism.

Our proposed GECIs should work by bioluminescence resonance energy transfer (BRET) when using bioluminescence as light sources. BRET follows the same physical rules as Förster resonance energy transfer (FRET). Thus, solid experimental evidence should be provided to support this mechanism.

3. Evaluate the bioluminescence enhancement of coordinating Au nanoparticles with sbGLuc of luminopsin on HEK293 cell membrane and determine the best working conditions (*i.e.* size and concentration of Au nanoparticles, and conjugation strategy).

LSPR can both enhance absorption and scattering of incident light, whereas only scattering can amplify the overall emission intensity. The ratio of scattering versus absorption in LSPR mainly depends on the size, shape, &

surface chemistry of Au nanoparticles, the dielectric constant of the medium environment, and the distance of an Au nanoparticle's surface to luciferase. LSPR of Au nanoparticles has been shown to be able to enhance bioluminescence of purified luciferase clusters, but Au nanoparticles have seldom been conjugated with luciferase expressed on the cell surface (*e.g.* the luciferase moiety of luminopsin). In order to obtain the best working conditions of our proposed Ni-NTA-Au conjugation strategy, the bioluminescence enhancement must be analyzed under various Au sizes, Au concentrations, and Au surface chemistry individually with proper control *in vitro*.

To date, no studies have attempted to provide GECIs that can function under both bioluminescence and fluorescence excitation. Since bioluminescence of GLuc only requires its cell membrane- and blood brain barrier-permeable substrate coelenterazine (CTZ), the working process of GECIs based on bioluminescence is less invasive *in vivo*, compared with other fluorescence based GECIs, which always require installation of optical fibers or exposure of the brain tissue to strong excitation light delivery. Also, because our GECIs are ratiometric indicators based on the ratio of peak wavelength of donor and acceptor domain, they yield more accurate and repeatable results that are independent of optical pathways and CTZ concentrations. Those parameters are practically hard to control *in vivo*.

Meanwhile, dim bioluminescence intensity is one restriction that limits sensitivity of many bioluminescence-based biosensors. Au nanoparticles have recently shown great potential in bioluminescence enhancement (Du et al., 2014). Thus, developing a simple and effective bioluminescence enhancement strategy using Au nanoparticles is strongly desirable.

The significance of the first part of this work stems from the persistent demand of accurate, sensitive, and noninvasive Ca^{2+} biosensors in cell biology studies. Ca^{2+} signaling cascade is a critical signal pathway in bone formation, muscle contraction, exocytosis, neuronal signaling, *etc.* Our bioluminescence based GECIs provide a novel tool for studying intracellular Ca^{2+} dynamics where target tissue is extremely fragile such as brain tissue. The significance of the second part of this work stems from the strong desire to improve bioluminescence intensity, where the sensitivity and activity of bioluminescent biosensors are restricted by dim bioluminescence. By exploiting LSPR of Au nanoparticle on bioluminescence enhancement,

bioluminescence should be more competitive in developing more sensitive and effective biosensors.

In the chapters that follow, a comprehensive background of my work was provided. In chapter 3, two BRET based GECIs were proposed. Then, the design of the two BRET based GECIs was fully detailed, and *in vitro* experiments were performed to test my design. At the end of this chapter, the results of the experiments were reported and discussed. The directions for future studies were suggested as well.

In chapter 4, the enhancement of bioluminescence of sbGLuc by gold nanoparticles (AuNPs) was presented. A strategy of conjugating hexahistidine tagged lumiopsins (LMOs) with Ni-NTA-Au complex to leverage LSPR on Au surface to enhance bioluminescence on cell surfaces was proposed. Then, the design of three his-tagged LMOs was fully detailed, and *in vitro* experiments to test their performance were performed. At the end of this chapter, the results of the experiments were reported and discussed, and the direction for future studies was suggested. In the last chapter, the results of chapter 3 and 4 were summarized, and the importance of this study was restated.

CHAPTER 2 LITERATURE REVIEW

2.1 General Characteristics of Ca^{2+} Indicator

Generally speaking, Ca^{2+} indicators exhibit altered fluorescent properties that depend on Ca^{2+} binding. Based on their chemical origin, Ca^{2+} indicators can be categorized into two classes: chemically synthesized indicators and genetically encoded indicators. An important thing to note is that Ca^{2+} indicators bind and interact only with free Ca^{2+} ions. In this light, the majority of intracellular Ca^{2+} is not free to diffuse but tightly chelated with various cytosolic buffers. The equilibrium of bound Ca^{2+} and free Ca^{2+} varies in different cell types as well as in various compartments of a cell. Roughly speaking, in every 100 cytosolic Ca^{2+} ions, only 1 Ca^{2+} ion is free to diffuse. This ratio is of the order of 10 to 1 within the endoplasmic reticulum (Li & Camacho, 2004; Raeymaekers, 1998). Since Ca^{2+} indicator itself also chelates Ca^{2+} , it can impact both the levels and most noticeably, the kinetics of Ca^{2+} signaling within cells. Thus, users have to carefully consider not only the spectral characteristics of a chemical indicator (*e.g.* whether it fluoresces in the red or green spectrum), but also pay close attention to its Ca^{2+} binding properties (Paredes, Etzler, Watts, Zheng, & Lechleiter, 2008).

In order to choose the most appropriate Ca^{2+} indicator to fit your study needs, there are several aspects that need to be considered, detailed in Paredes et al. (2008)'s review. Here are some major concerns which will be discussed below. First, users need to choose indicators with appropriate Ca^{2+} affinities. Since the Ca^{2+} indicator itself can bind with free Ca^{2+} that could significantly affect Ca^{2+} signaling. Therefore users must balance the trade-off of increasing the strength of the indicator signal with increasing concentration and affinities of indicators. In some cases, indicators with low Ca^{2+} affinities are required to reduce the impact of buffering of the indicator itself, but this also pays the cost of signal strength. Second, spectral properties of indicators need to be considered, as ratiometric and intensimetric indicators have their own strengths and weaknesses. Third, specifically for synthetic Ca^{2+} indicators (dyes), users need to choose the proper form of the dyes, since it decides the following loading procedures. These criteria are generally applicable for both synthetic Ca^{2+} indicators and genetically encoded Ca^{2+} indicators.

2.1.1 Ca²⁺ Affinities

Chemically speaking, Ca²⁺ affinities of indicators can be depicted by classical ligand-macromolecule interaction model mathematically. Let I stand for the indicator with x binding sites of free Ca²⁺, and L stands for the ligand free Ca²⁺ ion, as shown in equation 2-1. Such ligand-macromolecule saturation process can be depicted by the Hill equation (equation 2-2), where θ is the fraction of the indicator concentration that is bound to Ca²⁺. The apparent dissociation constant (K_d), as defined in the equation 2-3, describes how tightly an indicator binds free Ca²⁺ ions. The hill coefficient n describes cooperativity of the binding process, of which is normally bigger than 1 for Ca²⁺-calmodulin interaction (Chen et al., 2013). The binding process with >1 hill coefficient is called positive cooperative binding, of which one ligand molecule bound to the enzyme facilitate following ligand binding to other sites. It is worth to note that the hill coefficient n rarely equals the number of binding sites x on macromolecules, instead can be interpreted as an “interaction coefficient” describing the cooperativity among ligand binding sites. From definition of K_d , it has molarity units (M) and equals the ratio of k_a (forward rate, or the rate of association of the indicator-Ca²⁺ complex) and k_d (reverse rate, or the complex's rate of dissociation). K_A is equal to the concentration of free Ca²⁺ at which half of the total indicator molecules are bound with Ca²⁺, which also called microscopic dissociation constant. Hence, since the hill coefficient n for Ca²⁺-calmodulin binding >1 , the lower K_d is, the less Ca²⁺ affinity the indicator has, and the more sensitive the indicator is. When possible, users should choose the indicators that targeting $[Ca^{2+}]$ to be measured is between 0.1 to 10 times their K_d (Paredes et al., 2008), because within this range, fluorescence changes of indicators are the largest. If K_d is too far away from $[Ca^{2+}]$ of working environment, GECIs will be either saturated or unbound, which leads to no signal response to $[Ca^{2+}]$ change.



$$\theta = \frac{[L]^n}{K_d + [L]^n} = \frac{[L]^n}{K_A^n + [L]^n} = \frac{1}{\left(\frac{K_A}{[L]}\right)^n + 1} \quad \text{eq. 2-2}$$

$$K_d = \frac{k_d}{k_a} = \frac{[I][L]^n}{[IL_n]} = (K_A)^n \quad \text{eq. 2-3}$$

It is important to note that K_d is also dependent on pH, temperature, viscosity, ionic strength, protein binding and the amount of Mg²⁺ and other ions present (Larsson, Larsson, Lundgren, & Sundell, 1999; Lattanzio, 1990; Oliver, Baker, Fugate, Tablin,

& Crowe, 2000; Woodruff et al., 2002). As the result, the K_d of certain indicator *in vivo* may not have the same value as the K_d *in vitro*. It may be even different at each subcellular compartment in the same cell type. Thus, to obtain accurate calibration result, it is necessary to measure K_d *in situ* each time ahead of the actual measurement. Most commonly, Ca^{2+} indicators will exhibit different emission spectrum under a series of equilibrated buffer with gradient $[\text{Ca}^{2+}]$ up to the indicator saturation. For single wavelength based Ca^{2+} indicators (see 2.1.2), their fluorescence emission at single wavelength F can be normalized to θ by $(F-F_{\min})/(F_{\max}-F_{\min})$, where F_{\max} and F_{\min} is the fluorescence emission at two $[\text{Ca}^{2+}]$ boundaries in calibration buffer, and fitted with the Hill equation (eq. 2-2) to obtain K_d and n . The K_d obtained in this way is the apparent dissociation constant, which is specific for the current emission wavelength. For ratiometric Ca^{2+} indicators, if we use similar strategy to normalize the ratio R of two wavelengths with $\theta = (R-R_{\min})/(R_{\max}-R_{\min})$ and fit into the Hill equation (eq. 2-2), the apparent K_d obtained is only comparable with other ratiometric Ca^{2+} indicators using the ratio of the same wavelengths. If a single wavelength Ca^{2+} indicator shares one same emission wavelength with a ratiometric Ca^{2+} indicator, the apparent K_d obtained above cannot be directly compared between the ratiometric and the single wavelength Ca^{2+} indicator, since the apparently K_d contains the systematic bias from that different emission wavelength. Grynkiewicz, Poenie, and Tsien (1985) derived a calibration equation of ratiometric indicators with Hill coefficient 1, which form a simple 1:1 complex with Ca^{2+} , assuming the indicator concentration and path length are small enough for the fluorescence contribution from any given molecular species to be proportional to the concentration of that species, which is generally true in most physiological conditions (Grynkiewicz et al., 1985). The K_d calculated from their equation is corrected to reflect the Ca^{2+} affinities under only one wavelength, which can be then compared with single wavelength Ca^{2+} indicator sharing the same emission wavelength, thus called the effective K_d . Here I will generalize this equation for indicators with any Hill coefficient n .

Using the same notation as in Grynkiewicz et al. (1985), two wavelengths and two species (free and Ca^{2+} bound indicators, simplified as indicators below) require four proportional coefficients, hereby symbolized as S_{f1} for free indicators measured at wavelength λ_1 , S_{f2} for free indicators at λ_2 , S_{b1} for Ca^{2+} bound indicators at λ_1 , S_{b2} for Ca^{2+} bound indicators at λ_2 . Under the assumption of proportional relation between the species concentration and their emission intensities,

$$F_1 = S_{f1}c_f + S_{b1}c_b \quad (1)$$

$$F_2 = S_{f2}c_f + S_{b2}c_b \quad (2)$$

where F_1 is the sum of the fluorescence emission contributed by the concentration c_f of free indicators at wavelength λ_1 and the fluorescence emission contributed by the concentration c_b of bound indicators at λ_1 , so do the similar definition for F_2 at wavelength λ_2 .

From the Hill equation (eq.2-2)

$$\theta = \frac{c_b}{c_f + c_b} = \frac{1}{\left(\frac{K_d}{[Ca^{2+}]}\right)^n + 1} \quad (3)$$

rearrange to get

$$c_b = c_f \left(\frac{[Ca^{2+}]}{K_d}\right)^n \quad (4)$$

which is applicable to indicators with any Hill coefficient n .

Also, the ratio R in ratiometric indicators is

$$R = \frac{F_1}{F_2} = \frac{S_{f1}c_f + S_{b1}c_b}{S_{f2}c_f + S_{b2}c_b} \quad (5)$$

Insert relation (4) into (5) to solve for R yields the following calibration equation

$$\left(\frac{[Ca^{2+}]}{K_d}\right)^n = \left(\frac{R - S_{f1}/S_{f2}}{S_{b1}/S_{b2} - R}\right) \left(\frac{S_{f2}}{S_{b2}}\right) \quad (6)$$

Note that S_{f1}/S_{f2} is simply the limiting value that R can have at zero $[Ca^{2+}]$ and so may be approximate as R_{min} , while S_{b1}/S_{b2} is the analogous limiting R_{max} that the ratio has at saturating $[Ca^{2+}]$. The above equation can be further converted to the linear form

$$\log \left[\left(\frac{R - R_{min}}{R_{max} - R} \right) \left(\frac{S_{f2}}{S_{b2}} \right) \right] = n \log [Ca^{2+}] - n \log K_d \quad (7)$$

where K_d is the effective dissociation constant that separates the systematic bias $\frac{S_{f2}}{S_{b2}}$ on K_d caused by emission wavelength λ_2 compared with the apparent K_d directly derived from the Hill equation containing the influence from $\frac{S_{f2}}{S_{b2}}$ at emission wavelength λ_2 .

$$\log \left[\left(\frac{R - R_{min}}{R_{max} - R} \right) \right] = n \log [Ca^{2+}] - \log K_d \quad (8)$$

Thus, the effective K_d of ratiometric indicators derived from (7) is comparable with the apparent K_d of single wavelength indicators derived from (8), where they share the same emission wavelength λ_1 .

2.1.2 Spectral Properties

Since all available Ca^{2+} indicators are based on fluorescence changes upon Ca^{2+} binding, the spectrum changes determine the final results and should be carefully considered. Generally, Ca^{2+} indicators can be categorized either single-wavelength (intensitymetric) or double-wavelength (ratiometric) indicators. Single wavelength indicators exhibit significant Ca^{2+} dependent changes in fluorescence intensity without shifting their relative excitation or emission spectrum (*e.g.* Figure 2-1). It is easier to avoid or minimize spectral overlap with other fluorophores when working with single wavelength indicators (Peter Lipp, Lüscher, & Niggli, 1996; P Lipp & Niggli, 1993; Nicotera & Rossi, 1994). However, for chemically synthesized indicators, the measuring variable is also affected by experimental procedures like uneven dye loading, dye leakage, photobleaching and changes in cell volume; for genetically encoded indicators, the measuring variable is affected by handling cell types, transfected cell numbers, expression levels, *etc.* Another class, ratiometric indicators shift the peak wavelength of either their excitation or emission spectrum upon binding Ca^{2+} . This class of indicators permit more accurate quantification of the free $[\text{Ca}^{2+}]$ compared with single wavelength indicators, because the measuring variable is unitless that only depends on the free $[\text{Ca}^{2+}]$.

Imaging equipment is another major consideration when choosing proper indicators. Obviously, kinds of indicators are limited by the corresponding excitation light sources. For single-photon laser scanning microscopes (1p-LSM), the excitation of indicators needs to match with the specific available lasers. When working with two-photon laser scanning microscopes (2p-LSM), the absorption properties of Ca^{2+} indicators can be significantly different than what might be predicted by simply doubling the peak of single photon absorption wavelength. Additional absorption peaks are frequently present at shorter wavelengths. Absorption curves can also be much broader for two-photon excitation, making it more difficult to exclusively excite an indicator at a single wavelength.

For conventional widefield epi-fluorescent microscope, the excitation of indicators is limited by the appropriate and specific filter set. If a widefield epifluorescence

microscope is used, the light source may also affect the performance of the indicators. The two most common lamp sources used in widefield epifluorescence microscopes are the mercury and xenon arc burners. Both are broad-spectrum emitters. However, mercury lamps do not provide an even intensity across the entire spectrum. The highest intensity peaks occur at 334, 365, 406, 435, 546 and 578 nm with steady lower intensity at wavelengths in between these values (Paredes et al., 2008). Xenon lamps have a relatively even intensity across the visible spectrum, but they are not as intense and are particularly lower in the ultraviolet.

Finally, auto-fluorescence comes from biomolecules (*e.g.* NAD(P)H and flavin) and materials to hold the fluorescent specimen (*e.g.* plastic cultureware) must be distinguished and subtracted from indicators fluorescence signal. When signal-to-noise ratio is high, *e.g.* background signal is less than 10% of total signal, after subtracting the background signal, measuring variable can keep good dependency with free $[Ca^{2+}]$. However, when background signal is too high, *e.g.* higher than 80% of total signal, even after subtracting the background, the measuring variable may lose dependency on free $[Ca^{2+}]$.

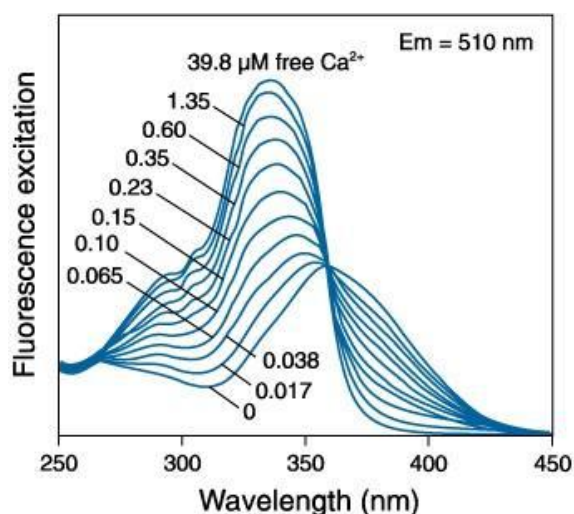


Figure 2-1 Excitation spectrum of Fura-2 dye measured at emission wavelength of 510 nm with free Ca^{2+} from 0 – 39.8 μM . Two excitation peaks were seen around 340 nm and 380 nm wavelength. The excitation peak for 340nm increases with increase in $[Ca^{2+}]$ whereas the excitation peak for 380nm decreases with increase in the $[Ca^{2+}]$.

2.1.3 Indicator Forms

Chemical forms of Ca^{2+} indicators are the concerns of chemically synthesized Ca^{2+} indicators, since different forms will directly affect the loading procedures, targeting

efficiency and possible compartmentalization. Generally, there are three common chemical forms that are available commercially: salts, dextran conjugates or acetoxymethyl (AM) esters. More detailed discussion can be found in Paredes et al. (2008)'s review. One major advantage of genetically encoded Ca^{2+} indicators are that they can be specifically targeted to interested subcellular site by noninvasive means like cell-type specific promoters, cellular targeting sequences, transgenic technology, *etc* (Akerboom et al., 2013; Marco Mank et al., 2008; Tian et al., 2009).

2.2 Chemically Synthesized Ca^{2+} Indicator

The measurement of intracellular $[\text{Ca}^{2+}]$ first became practical and common after chemically synthesized Ca^{2+} indicators (or commonly called dyes) were developed. Thanks for the work of Roger Y. Tsien, who generated a series of fluorescent polycarboxylate compounds with strongly improved fluorescence properties. Nowadays, there are a broad range of Ca^{2+} affinities that are commercially available for the users, and protocols of utilizing these dyes *in vivo* and *in vitro* are well established (Rehberg, Lepier, Solchenberger, Osten, & Blum, 2008). Here I tabulate some common commercial dyes with high sensitivity (high affinities) in Table 1.

Table 1 High affinity chemically synthesized Ca^{2+} sensors

Indicator	K_d ($[\text{Ca}^{2+}]$, nM)	Excitation (nm), emission (nm)	Notes
Calcium Green-1	190	490 ex, 531em	Single wavelength
Fluo-3	325	506 ex, 526 em	Single wavelength
Fluo-4	345	494 ex, 516 em	Single wavelength
Fura-2	145	363&335 ex, 512 em	Dual excitation/single emission
Indo-1	230	488 ex, 405&485 em	Single excitation/dual emission
Oregon Green 488 BAPTA-1	170	488 ex, 520 em	Single long wavelength

Table 1 (continued).

Fura-4F	0.77	336/366 ex, 512 em	Ratiometric excitation/single emission
Fura-5F	0.40	336/363 ex, 512 em	Ratiometric excitation/single emission
Calcium Crimson	185	590 ex, 615 em	Single long wavelength
X-rhod-1	0.7	580 ex, 602 em	Single excitation/emission

2.3 Genetically Encoded Ca^{2+} Indicator

Since synthesized Ca^{2+} indicators face great difficulty in dye loading process, controllable compartmentalization and diffusion and specific labeling at subcellular level like pre- or postsynaptic sites, genetically encoded Ca^{2+} indicators (GECIs) are proposed to address these problems. So far, the fluorescence of known native fluorescent proteins (XFPs, *e.g.* GFP) is in general insensitive to fluctuation of $[\text{Ca}^{2+}]$. To confer XFPs Ca^{2+} sensitivity, GECIs fuse Ca^{2+} binding protein motifs and XFPs with their mutants to translate Ca^{2+} signal to light signal and detect by imaging devices. There are two successful paradigms of constructing GECIs: FRET (Förster resonance energy transfer) between two mutated XFPs, and Ca^{2+} mediated modulation of a single XFP. In the following section, designing concerns of GECIs will be discussed and representative examples will be given for each group.

2.3.1 Ca^{2+} binding protein motifs

In nature, there exists a variety of Ca^{2+} binding sites in proteins, but only two prominent types of intracellular Ca^{2+} binding motifs that can coordinate Ca^{2+} in the physiologically relevant range (Hilge, Aelen, Perrakis, & Vuister, 2007; Moldoveanu, Jia, & Davies, 2004). These motifs are C2 domains and EF-hands. C2 domains have been found in a huge number of different proteins, *e.g.*, PLA₂ (phospholipase A2), PLC (phospholipase C), PKC (protein kinase C), and synaptotagmin (Rizo & Südhof, 1998). One characteristic of many C2 domains are that they bind Ca^{2+} and phospholipids, though some variants evolve to bind other targets. For example, phospholipid can act as a ligand for calcium binding in PKC-C2 domain, and it will

increase the affinity for Ca^{2+} binding. Another C2 domain, C₂A domain of synaptotagmin I, the K_d of Ca^{2+} binding can be decreased 1000-fold in the presence of phospholipids (Rizo & Südhof, 1998). Due to those interrelationship between phospholipids and Ca^{2+} , C2 domains are not a first choice in most GECIs design.

In contrast to C2 domains, EF-hands have Ca^{2+} as its only ligand. EF-hands have a helix-loop-helix motif of ~30 amino acids and usually form dimer, tetramer, hexamer or more protein complex. The most important part is the loop regions which give rise to the coordination space through predominantly negatively charged amino acid residues (Figure 2-2A).

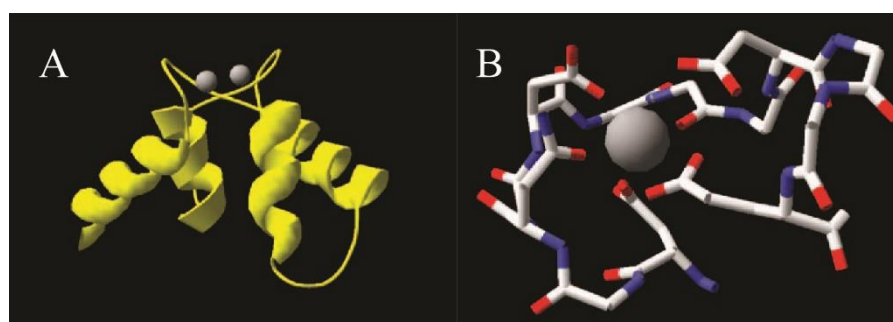


Figure 2-2 Structure of typical EF-hands and its Ca^{2+} binding center. (A) C-terminal EF-hand domain of chicken skeletal troponin C (csTnC, PDB file 1TOP, shown in yellow) complexed with two Ca^{2+} (shown in gray) (B) Blowup of the coordination in EF-hand III of csTnC (M. Mank & Griesbeck, 2008)

Most EF-hand-containing proteins (*e.g.*, troponin C & calmodulin) possess the so-called canonical EF-hand. This version of the domain exhibits a 12-residue calcium-binding loop consisting of nine residues in the loop region and three residues in the exiting helical part of the EF-hand (Figure 2-2B). For example, calmodulin forms two globular domains connected by a flexible central linker. Each domain binds two calcium ions in EF hand motifs, so that calmodulin can bind a total of four Ca^{2+} ions. The canonical EF-hand coordinates Ca^{2+} via a pentagonal bipyramid, *i.e.*, through seven coordinating partners. The positions inside the 12-residue binding loop are referred as 1 (+X), 3 (+Y), 5 (+Z), 7 (-Y), 1 (-X), 12 (-Z). The numbers inside the position along the linear sequence of the loop, whereas letters indicate the position in the 3D geometry of the pentagonal bipyramid (Figure 2-3).

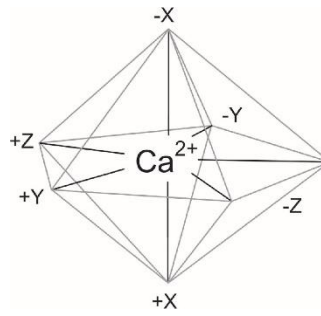


Figure 2-3 Schematic of the Ca^{2+} coordination in a canonical EF-hand. Letters are positions of the residues that are involved in the Ca^{2+} coordination. Note that two ligands in the planar pentagon are provided by the same amino acid residue (-Z). (M. Mank & Griesbeck, 2008)

According to functions of EF-hand containing proteins, EF-hand motifs can be categorized into two kinds: “regulatory” EF-hands that undergo a conformational change after calcium binding and “structural” EF-hands that do not (Grabarek, 2006). The regulatory hands are typical of proteins with important regulatory functions such as calmodulin (CaM), troponin C (TnC), and recoverin. These proteins typically mediate Ca^{2+} related physiology and biochemistry of a cell. Calmodulin forms two globular domains connected by a flexible central linker. Each domain binds two calcium ions in EF hand motifs, a motif ubiquitous in calcium-binding proteins, so that calmodulin can bind a total of four Ca^{2+} ions. The structural hands are found in buffer proteins such as calbindin D9K or parvalbumin which serve to shape the profile and duration of calcium signals within cells (M. Mank & Griesbeck, 2008).

Since EF-hands motif commonly form pairs in proteins, they tend to stack against each other and improve mutual stabilization. As a consequence, calcium binding to EF-hands are often cooperative. In general, the first Ca^{2+} binding to EF hands will facilitate following Ca^{2+} binding due to favorable conformational change. Thus, most EF hands have positive cooperative Ca^{2+} binding kinetics. Last thing to note is that same as the chemically synthesized Ca^{2+} indicators, K_d of Ca^{2+} binding motifs usually depend on pH and concentration of other ions (*e.g.* Mg^{2+} , Cl^-), hence it requires calibration each time before the real measurement (Palmer & Tsien, 2006).

2.3.2 FRET-based GECIs

Förster resonance energy transfer (FRET) is a spectroscopic phenomenon that the excited donor fluorophore transfers its excitation energy non-radioactively to a proximal ground-state acceptor fluorophore (Clapp, Medintz, & Mattoussi, 2006).

FRET is sensitive to changes in conformation, orientation and distance between donor and acceptor. The efficiency of FRET can be quantitatively described by the Förster equation (eq. 2-4), and it decreases sharply with increasing distance between donor and acceptor (Figure 2-4). In the equation, r is the actual distance between the

$$E_{\text{FRET}} = \frac{R_0^6}{R_0^6 + r^6} \quad \text{eq. 2-4}$$

fluorophores, and R_0 is the distance at which energy transfer between a given donor-acceptor pair is half-maximal (also called Förster distance). It should be noted that R_0 is a specific value for each individual donor-acceptor pair that depends on spectral overlap between donor emission and acceptor excitation, the donor quantum yield, and an orientation factor κ^2 . Typically, Förster distances are in the range of 20-80 Å. Using Ca^{2+} binding motif to control the distance and orientation between donor and acceptor, FRET has been extensively exploited as GECIs. As mentioned in the section 2.3.1, calmodulin (CaM) and troponin C (TnC) are two most commonly used Ca^{2+} binding motifs. Due to the interest of my work, most examples shown below will be based on CaM. The examples employing TnC can be found in Mank and Griesbeck's review (2008).

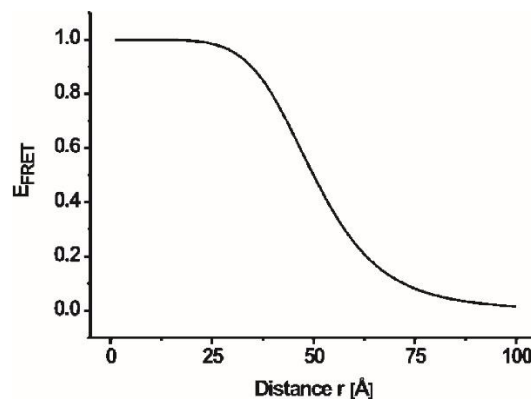


Figure 2-4 Dependency of FRET efficiency (E_{FRET}) on the distance (r) between a donor-acceptor pair with an assumed Förster radius R_0 of 50 Å. Note that the relationship is only linear with distance changes in the vicinity of R_0 . Therefore an idealized, approximately linear FRET reporter will preferably operate at E_{FRET} values between 0.2 and 0.8. (M. Mank & Griesbeck, 2008)

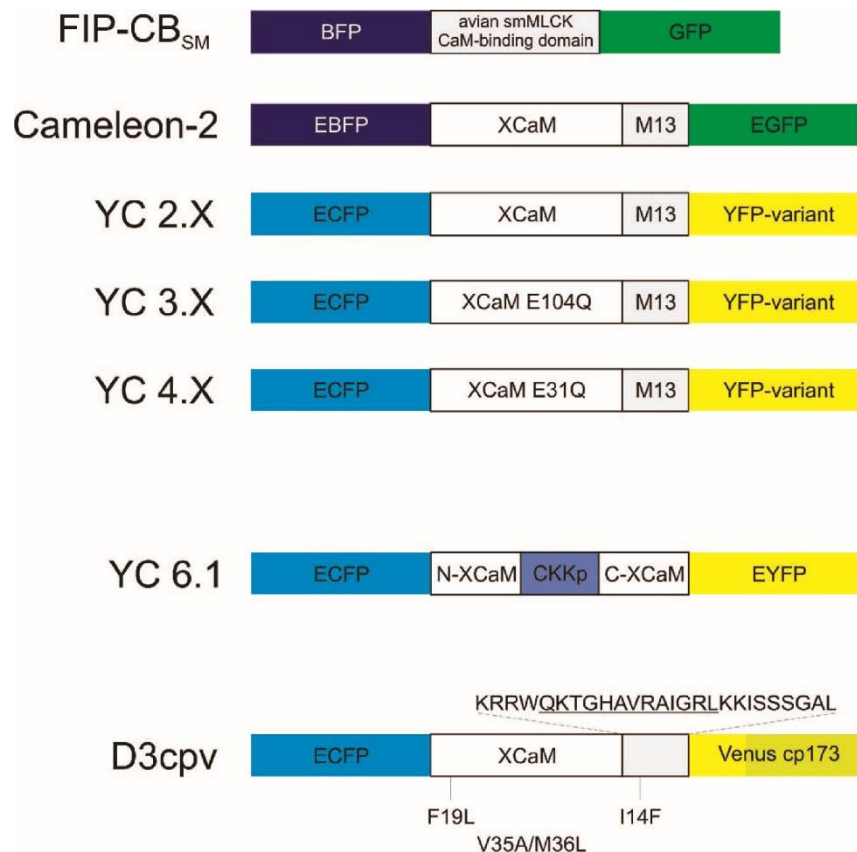


Figure 2-5 Calmodulin (CaM)/FRET-based GECIs (M. Mank & Griesbeck, 2008). See text for detail.

One famous example is a group of GECIs called “Cameleons”. They utilize CaM and its binding peptide M13 from myosin light chain kinase as Ca²⁺ binding motif which sandwiched by enhanced blue fluorescent protein (EBFP) and enhanced green fluorescent protein (EGFP) (Figure 2-5). Upon Ca²⁺ binding to CaM, Ca²⁺/CaM is thought to wrap around the neighboring M13 peptide, thereby initiating a conformational change of CaM and bringing donor (EBFP) and acceptor (EGFP) to proximity, which increases FRET efficiency of the donor-acceptor pair in a manner of Ca²⁺ dependency. The reasoning for including the CaM-binding motif was first of all to increase conformational change of the protein complex. Second, the preferred intramolecular interaction of CaM with a flanking binding peptide was thought to prevent activating of CaM-dependent target proteins within a cellular environment. Early version of Cameleons uses BFP (or its mutant Enhanced BFP) as its donor, but it turned out that BFP were not suitable for live cell imaging, as they are dim and bleached rapidly. Therefore, the donor-acceptor pair was switched to cyan fluorescent protein (CFP) and yellow fluorescent protein (YFP) in yellow Cameleon 2.0 (YC2.0),

which obtains higher signal-to-noise ratio and more stable imaging in live cells at the cost of slightly higher spectral overlap of the CFP emission with the YFP emission band (A. Miyawaki et al., 1997). Tuning Ca^{2+} affinities can be achieved by site directed mutagenesis of chelating residues within EF-hand motifs of CaM (A. Miyawaki et al., 1997). Cameleon-2 with wild-type CaM was reported to have biphasic Ca^{2+} dependency with K_d 's of 70 nM and 11 μM , substitutes glutamate 104 with glutamine located at the third Ca^{2+} binding loop of CaM resulted in Cameleon-3 (YC 3.X) with a lower affinity K_d of 4.4 μM , while the mutation E31Q in Cameleon-4 (YC 4.X) shifted affinities to K_d 's of 83 nM and 11 μM (A. Miyawaki et al., 1997). A problem of Cameleons is they have a small dynamic range, making subtle changes in $[\text{Ca}^{2+}]$ difficult to detect in some cells and organelles. Thus, in Cameleon-6 (YC6.X), CaM was split, and the CaM binding peptide derived from CaM-dependent kinase kinase (CKKp) was inserted to replace M13, which YC 6.1 displays a two-fold dynamic range increase at $[\text{Ca}^{2+}]$ from 0.05-1 μM (Truong et al., 2001). While CFP fluorescence remains relatively stable down to approximately pH 6, another line of improvement consisted in replacing YFP as acceptor. The first version of YFP has a pK_a of 7.0, and it is too sensitive to small pH fluctuation in the cytosol which can range from 6.8 to 7.3 under various condition. Meanwhile, YFP is easily to be quenched by Cl^- under physiological condition. Therefore, other variants of YFP were needed so that donor-acceptor fluorophores are insensitive to common physiological factors and only mediated by FRET.

A first remedy was replacing YFP with YFP-V68L/Q69K in YC 2.1, which had a pK_a of 6.1 (Atsushi Miyawaki, Griesbeck, Heim, & Tsien, 1999). Later the YFP variant, Citrine, with the mutation Q69M showed better results, which pK_a was further shifted to 5.7 and also insensitive to chloride concentrations (Griesbeck, Baird, Campbell, Zacharias, & Tsien, 2001). Subsequently another YFP variant called Venus in YC 2.3/3.3/4.3 or YC 2.12 also exhibited less pH and Cl^- sensitivity (Griesbeck et al., 2001; Nagai et al., 2002). The most significant improvement was the development of circular permutation of GFP and its variants (cpXFPs). cpXFPs result from interchange of amino and carboxy portions of the wild-type XFP (Figure 2-6). The original N- and C- termini are linked via a short peptide sequence so that new N- and C- termini become available for fusing fluorophore to the Ca^{2+} binding motifs. Incorporating a circular permuted form of Venus (Venus cp173) as an acceptor into YC 2.60/3.60 resulted in a more than 5-fold dynamic range increase in emission ratio

in vitro from zero to saturated Ca^{2+} (Nagai, Yamada, Tominaga, Ichikawa, & Miyawaki, 2004).

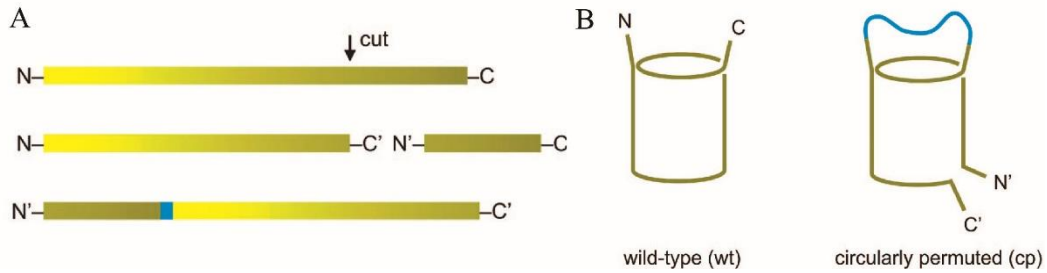


Figure 2-6 Circular permutation of GFPs. (A) Circularly permuted (cp) variants are obtained by opening of the wild-type protein sequence at an additional site. The resulting fragments are interchanged and combined (permuted) by a short linker (in blue), which fuses the original N- and C- terminus. A number of permutations are possible in this way that can result in functional fluorophore. (B) Circularly permuted proteins are thought to display the same 3D structures as their wild-type counterparts but have new N- and C- termini. (M. Mank & Griesbeck, 2008)

2.3.3 Single fluorophore-based GECIs

After a surprising discovery by Baird et al., that the β -barrel of GFP tolerated the insertion of large protein fragments without destroying fluorescence, it became feasible that using Ca^{2+} binding motifs to cause Ca^{2+} -dependent single fluorophore conformation change. One widely used GECIs of this kind is GCaMP and its updates. In GCaMP, the N-terminus of cpEGFP was connected to M13 peptide, which is a target sequence of CaM, whereas the C-terminus of cpEGFP was connected to CaM (Figure 2-7). The cpEGFP in GCaMP was created by connecting the original EGFP terminus with amino acid sequence “GGTGGG” and deleting amino acid residues 145-148 to make new N and C terminus (Figure 2-7A). When Ca^{2+} binds to CaM, conformational changes due to the Ca^{2+} -CaM-M13 interaction induce a subsequent conformational change in cpEGFP, therefore fluorescence intensity increases. As it turned out, the linker sequences used to fuse M13 and CaM to the cpEGFP moiety are crucial for tuning response properties of GCaMP. Numerous rounds of structure-guided optimization have been employed to improve sensitivity and provide various Ca^{2+} affinities (Chen et al., 2013; Hilge et al., 2007; Remington, 2006). So far, the latest version GCaMP6 provides great dynamic range, high Ca^{2+} affinity and three different binding kinetics (fast, medium and slow) (Table 2).

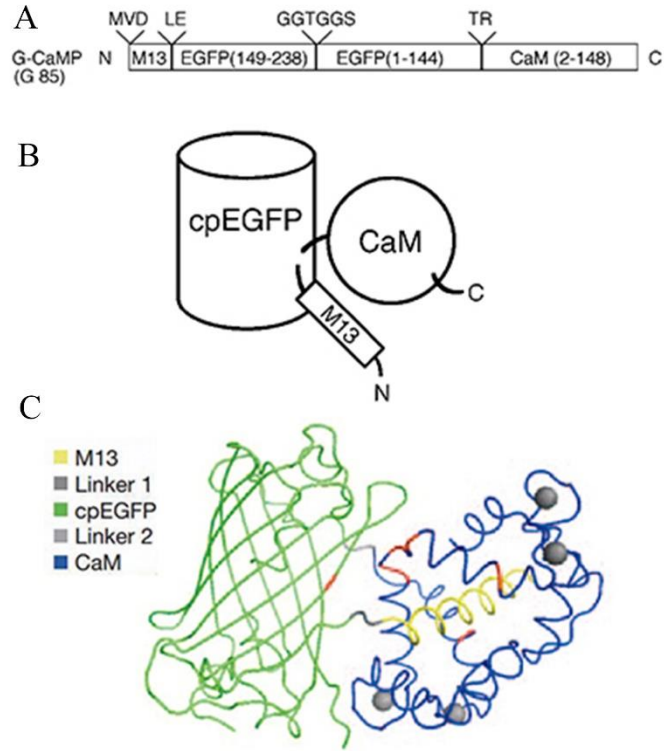


Figure 2-7 Schematic representation of GCaMP and its crystal structure. (A) GCaMP consists of the M13 (myosin light chain kinase), cpEGFP (circularly permuted enhanced GFP) and CaM (calmodulin) located N to C terminally. (B) Schematic topology of GCaMP. (C) Crystal structure of GCaMP. (Chen et al., 2013)

Table 2 Comparison of Biochemical Properties of Purified GCaMP series sensors.

Sensor	Dynamic range (F_{\max}/F_{\min})	K_d (nM)	Hill coefficient	K_{off} (s^{-1})	pK_a , apo	pK_a , sat
GCaMP3	13.5 ± 0.7	345 ± 17	2.54 ± 0.04	2.57	8.44 ± 0.01	7.13 ± 0.07
GCaMP5G	45.5 ± 0.9	447 ± 10	2.46 ± 0.04	2.52	8.61 ± 0.15	6.58 ± 0.02
GCaMP6s	63.2 ± 3.1	144 ± 4	2.90 ± 0.17	1.12	9.77 ± 0.70	6.20 ± 0.02
GCaMP6m	38.1 ± 1.8	167 ± 3	2.96 ± 0.04	2.06	8.68 ± 0.09	6.90 ± 0.04
GCaMP6f	51.8 ± 2.8	375 ± 14	2.27 ± 0.10	3.93	8.77 ± 0.16	6.34 ± 0.01

2.4 Localized Surface Plasmon Resonance (LSPR)

First, some physical concepts used below will be briefly explained. Plasmon is a physical concept (quasiparticle) to describe plasma oscillation, or in our case, the oscillation of surface conduction electrons on certain material surface. The materials that possess a negative real and small positive imaginary dielectric constant (usually metal) are capable of supporting a surface plasmon resonance (SPR). This resonance is a coherent oscillation mode which comprise an electromagnetic (EM) field coupled to the oscillations of surface conduction electrons. Surface plasmon refers to the oscillations of the surface conduction electrons excited by electromagnetic radiation, i.e., incident light. When the material is at a bulk scale (*e.g.* larger than micron), plasmons propagate in the x- and y- directions along the material-dielectric interface, for distances on the order of tens to hundreds of microns, and decay evanescently in the z-direction (perpendicular to the film) with $1/e$ decay lengths on the order of 200 nm (Figure 2-8 A). When the size of the material shrinks into nanoscale, plasmon oscillates locally around the nanoparticle with a frequency known as the localized surface plasmon resonance (LSPR) (Figure 2-8 B). Both SPR and LSPR are sensitive to changes in the local dielectric environment and has been studied in several surface enhancement phenomena: surface-enhanced Raman scattering (SERS), hyper-Raman scattering, one- and two-photon absorption, second harmonic generation (SHG), and surface-enhanced luminescence/fluorescence.

For many metals such as Pb, In, Hg, Sn, and Cd, SPR frequency lies in the UV part of the spectrum and nanoparticles do not display strong enhancement effects. Such small metal particles are also readily oxidized making LSPR application infeasible. The coinage elements are exceptional. First, they are more noble and form air-stable colloids. Second, due to d-d band transition, the plasma frequency is pushed into visible part of the spectrum, which makes bioluminescence enhancement possible. Theoretically, both SPR and LSPR can be well depicted by Mie's theory (Mie, 1908). A full theoretical treatment of LSPR is beyond the scope of this review, which I would like to refer the interested reader to the Supplemental Appendix of Willets and Van Duyne's review (2007). For my thesis purpose, we consider a spherical nanoparticle of radius a that is irradiated by z-polarized light of wavelength λ (where a is much smaller than the wavelength of light λ ; i.e., $a/\lambda < 0.1$). In this limit, we can

calculate the extinction spectrum¹ of the metal sphere as follows (Willels & Van Duyne, 2007):

$$E(\lambda) = \frac{24\pi^2 N a^3 \varepsilon_{out}^{3/2}}{\lambda \ln(10)} \left[\frac{\varepsilon_i(\lambda)}{(\varepsilon_r(\lambda) + \chi \varepsilon_{out})^2 + \varepsilon_i(\lambda)^2} \right] \quad (\text{eq. 2-5})$$

Here, ε_r and ε_i are the real and imaginary components of the metal dielectric function, respectively, ε_{out} is the dielectric constant of the external environment, χ is the geometrical factor which is 2 for the case of a sphere, and N is the particle number which are excited by external light. From equation 2-5, we can learn that the frequency of LSPR depends not only on particle properties (shape, metal dielectric function, and particle number), but also on dielectric constant of the medium as well. Nanospheres, nanorods and silica-gold nanoshells are the most commonly used gold nanoparticles. By increasing the size of gold nanospheres from 20 to 80 nm, the magnitude of extinction as well as the relative contribution of scattering to the extinction rapidly increases (Jain, Lee, El-Sayed, & El-Sayed, 2006). For non-spherical nanoparticles, the extinction properties are determined by aspect ratio and the orientation of the external electric field relative to the particle as well (Liz-Marzan, 2006). As the equation 2-5 showed, LSPR is also affected by the surrounding medium of nanoparticles, which can be reflected by its refractive index, n . Under dilute nanoparticle dispersion presumption, Mie theory predicts the resonance occurs when $\varepsilon_1(\omega) = -2\varepsilon_m$ ($\varepsilon_1(\omega)$ being the real component of the metal dielectric function at angular frequency ω , and ε_m the medium dielectric constant. However, when nanoparticle is concentrated, the situation will become more complicated since interactions between neighboring particles can arise (Miller & Lazarides, 2005).

¹ Extinction spectrum: Absorption plus elastic light-scattering spectrum.

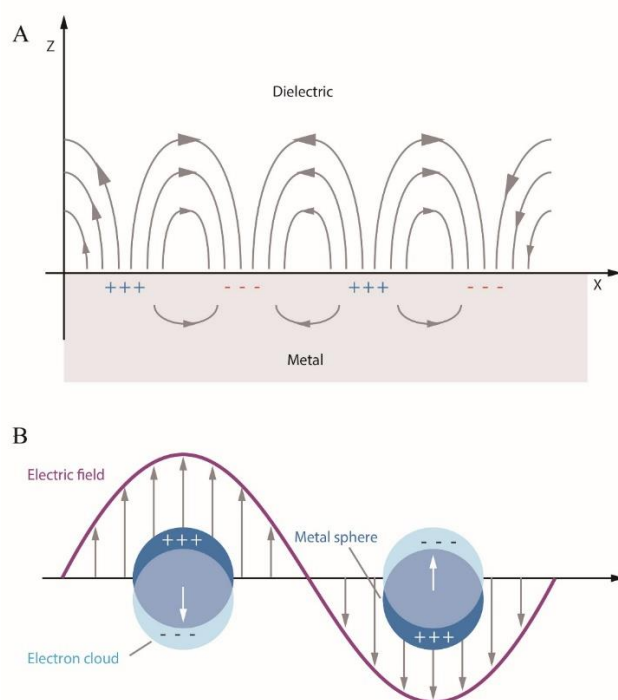


Figure 2-8 Schematic diagrams illustrating (A) a surface plasmon polariton (or propagating plasmon) and (B) a localized surface plasmon.

2.5 Gold Nanoparticle (AuNP) and Protein Conjugation

When AuNPs are exposed to protein solution, proteins are easily absorbed onto the surface of AuNPs to form a protein corona around AuNPs, which reduces the surface free energy of AuNPs. For example, AuNPs have been shown to absorb a variety of proteins such as ubiquitin (Tavanti, Pedone, & Menziani, 2015), serum albumin (Dominguez-Medina, McDonough, Swanglap, Landes, & Link, 2012), tumor necrosis factor (Tsai et al., 2012), cytochrome C (Aubin-Tam & Hamad-Schifferli, 2005), fibrinogen (Deng, Liang, Toth, Monteiro, & Minchin, 2012), *etc.* Different proteins have different binding site and binding affinities. Corona can be roughly divided into two types: hard and soft corona (P. Wang et al., 2015). Hard corona means that proteins are bound to the surface durably and tightly. In contrast, soft corona indicates that proteins are less tightly bound to the surface, which is dynamic and will exchange with proteins in the media with time (Milani, Baldelli Bombelli, Pitek, Dawson, & Rädler, 2012). When solution contains various proteins, the high abundance proteins first arrive at and bind on the surface of AuNPs to form soft corona, however, they will be eventually replaced by high-affinity proteins to form hard corona NP-proteins complexes (Rahman, Laurent, Tawil, Yahia, & Mahmoudi, 2013). Both chemical and

physical absorption take part in the formation of protein corona such as coordination, hydrogen bonding, Van der Waals forces, and hydrophobic interactions. For instance, when bovine serum albumin (BSA) interacts with AuNPs, the disulfide bonds of BSA absorb on the surface of AuNPs via at least 12 Au-S bonds (L. Wang et al., 2013). In contrast, ubiquitin is a small, cysteine free protein bound to citrate-coated AuNPs mainly via short-range, non-electrostatic interactions, such as hydrogen bonds, where the NH group binds to the central carboxylate group of surface citrate on AuNPs (Brancolini, Kokh, Calzolari, Wade, & Corni, 2012). There are three important factors that mediate the protein corona formation: AuNP size, hydrophobicity and surface chemistry.

2.5.1 AuNP size

The size of AuNPs determines the possible total amounts of absorbed proteins on the surface, since the size of AuNPs governs the curvature of AuNPs that have different protein binding constants. For example, polyacrylic acid (PAA)-coated AuNPs have negative charges on the surface and their sizes range from 7 nm to 22 nm. The binding affinities of the AuNPs to fibrinogen increases with the size of AuNPs (Deng et al., 2012). A similar study also showed that AuNPs ranging from 5 to 100 nm can interact with common human blood proteins including albumin, fibrinogen, globulin, histone, and insulin in a size-dependent manner, which indicates AuNPs with increasing sizes have stronger capability of binding to the proteins. They also suggested that the proteins undergo conformational change upon association with AuNPs, and that the thickness of the absorbed protein layer (size of AuNPs <50 nm) progressively increases with the AuNP sizes (Lacerda et al., 2009). Another team used gel electrophoresis and a combination of matrix-assisted laser desorption/ionization and time-of-flight mass spectrometry to quantitatively analyze and identify the mouse serum proteins absorbed on 5, 15 and 80 nm phosphine stabilized AuNPs with negative surface charges. They found smaller AuNPs have lower protein absorption than larger AuNPs because the former has a higher curvature that reduced the protein binding capacity (Schäffler et al., 2013).

2.5.2 Hydrophobicity

Hydrophobicity or hydrophilicity of AuNPs are crucial factors to mediate the composition and amount of protein absorption. A clean surface of gold is hydrophilic

(Bewig & Zisman, 1965). Hydrophobicity of AuNPs can be tuned by multiple surface modifications. For example, after modification with high density of hydrophilic polyethylene glycols (PEGs), AuNPs can resist the absorption of plasma proteins such as complement components (Fischer & Chan, 2007). In addition, AuNPs can be modified by both hydrophilic and hydrophobic thiolated ligand molecules, and by tuning their ratio, such surface heterogeneity can serve as a tunable property to modulate the conformation of absorbed proteins (Huang, Carney, Ikuma, Stellacci, & Lau, 2014). Moreover, for the same AuNPs, when compared with their hydrophilic counterparts, hydrophilic AuNPs can absorb more proteins from blood plasma (Lindman et al., 2007).

2.5.3 Surface chemistry

Pure AuNPs are not stable enough due to high surface free energy, thus, the surface of AuNPs is usually capped with citrate, cetrimonium bromide (CTAB), polyethylene glycol (PEG), silica or silica-PEG to increase their dispersibility and functionality. Surface chemistry not only affects the quality of AuNPs (stability, monodispersity, and biocompatibility) but also provides functional groups ($-\text{COO}^-$, $-\text{NH}_3^+$, $-\text{CHO}$, *etc.*) or charges that can be exploited for bioconjugation or ligand exchange. For example, the amount of protein absorbed on the PEGylated AuNPs depend on both the size of the AuNPs and the density of grafted PEG. Specially, the greater the PEG coating density, the smaller the amount of absorbed proteins on the surface (Walkey, Olsen, Guo, Emili, & Chan, 2012). Since Au can form many charge-neutral complexes, these Au chemistries have been extensively used in the surface modification of AuNPs to specifically conjugate with other biomolecules. For example, a wide range of molecules can be tethered onto the AuNPs surface by means of thiol ($-\text{SH}$) group. Cysteine can easily conjugate to the AuNPs through Au-S bond. After mutated to present an exposed cysteine residue, a single chain Fv antibody fragment (scFv) can form a gold-thiolate bond efficiently with AuNPs by chemical oxidation (Ackerson, Jadzinsky, Jensen, & Kornberg, 2006). Triphenylphosphine can also form coordination complex with Au. Triphenylphosphine can be synthesized with nitrilotriacetic acid (NTA) before coordinate with AuNPs, and the subsequent NTA-AuNPs can bind with histidine through nickel chelating system (Hainfeld, Liu, Halsey, Freimuth, & Powell, 1999).

CHAPTER 3 ULTRASENSITIVE BIOLUMINESCENT CALCIUM INDICATOR PROTEIN

3.1 Introduction

Although newly developed FRET based GECIs exhibited high sensitivity and excellent dynamic range, implantation of fiber optics or craniotomy (exposure of the brain through a glass coverslip or the thinned skull) is essential for their excitation *in vivo* (Chen, 2013). However, such implantation (normally inserted into brain tissue and affixed to the animal skull) still has several limitations, which could impair the results accuracy. For example, light emission can be visibly noticeable at the interface between the patch cable and the implanted optical fiber at high light-output intensities. If this is left unattended, it may serve as an unwarranted cue to the animal during behavioral sessions and may alter responses (Martin-Garcia et al., 2011). Other possible limitations include tissue damage during implantation, fibers breaking upon removal from brain tissue, and difficulties with long-term control (Sparta et al., 2011). Combining the distinct advantages of FRET and bioluminescence approaches would create unprecedented opportunities for monitoring intracellular Ca^{2+} level at a wide range of spatial and temporal scales. To allow noninvasive monitoring of $[\text{Ca}^{2+}]$ using light signal, we proposed two bioluminescence resonance energy transfer (BRET) based calcium indicators, GCaMPGLuc and GLucGCaMP; and one negative control, GCaMP2AGLuc, to prove the BRET mechanism of the indicators (Figure 3-1). *Gaussia* luciferase (GLuc; 185 aa, 19.9 kDa) is the smallest secreted luciferase known and is naturally secreted (Bornhop et al., 1999). The two BRET calcium indicators are fusion proteins composed of a “slow-burn” *Gaussia* luciferase (sbGLuc; M43L and M110L) (Welsh, Patel, Manthiram, & Swartz, 2009) without its native secretion signal and fluorescence based Ca^{2+} indicator GCaMP6s (Chen et al., 2013). When Ca^{2+} binding on M13 in GCaMP6s triggers conformational change in cpEGFP, the light generated by the luciferase as donor with coelenterazine (CTZ) will be transferred to excite cpEGFP as acceptor. This energy transfer between donor and acceptor is called BRET and obeys similar physical rules as FRET. The ratio of light emission of sbGLuc (donor) versus GCaMP6s (acceptor) will indicate the Ca^{2+} level. GCaMP2AGLuc, on the other hand possesses a T2A (*Thosea asigna* virus 2A) “self-cleaving” peptide sequence inserted between GCaMP6s and sbGLuc, where ribosome

skipping on the T2A sequence will release two separate translational products (Figure 3-2). Since BRET requires close proximity between donor and acceptor proteins for efficient energy transfer (see section 2.3.2), T2A sequence in GCaMP2AGLuc should interrupt this process and lose dependency with changing $[Ca^{2+}]$, which provides an important negative control of BRET mechanism of the two proposed indicators.

In this study, I will determine the K_d of GCaMPGLuc, GLucGCaMP and GCaMP2AGLuc under either BRET or fluorescence intracellular working condition *in vitro*. To accurately calibrate intracellular free $[Ca^{2+}]$, a series of standard EGTA-CaEGTA Ca^{2+} buffer mixed with ionomycin and nigericin will be used to equilibrate intracellular $[Ca^{2+}]$ with extracellular standard Ca^{2+} buffer solution (Petr & Wurster, 1997). Specifically, the equilibrium of EGTA mixing with CaEGTA ($K_d^{EGTA}=150.5$ nM at 20°C, pH 7.20, 0.1M KCl) in different ratios can generate a series of Ca^{2+} buffer with a similar range to typical intracellular $[Ca^{2+}]$ dynamics. Adding ionomycin and nigericin to this standard EGTA-CaEGTA buffer can then equilibrate intracellular $[Ca^{2+}]$ with the known extracellular standard Ca^{2+} solution. Ionomycin is a Ca^{2+} ionophore that is used to equilibrate the intracellular concentration with the known extracellular standard solution. Nigericin is a hydrogen ionophore used to maintain an intracellular proton concentration equal to the extracellular buffer solution. Thus, a stable intracellular environment is maintained in terms of ionic strength, temperature and pH.

There are several advantages of BRET-based GECIs compared with other GECIs. Using the ratio of two individual emission spectrum also improves the robustness as Ca^{2+} indicator compared with the single fluorescence emission spectrum of GCaMP6s, because the latter will be influenced by a variety of environmental factors (O'Connor, 2007), and requires more stringent *in situ* calibration, which will be tedious and challenging for some *in vivo* application (Chen, 2013). Also, the sbGLuc substrate, CTZ are highly hydrophobic molecules, hence easily to penetrate tissue barrier (*e.g.* blood brain barrier) to reach the targeted cells (Berglund, 2016). Since there is no obvious structure interference on GCaMP6s, the two BRET Ca^{2+} indicators should work both as a ratiometric bioluminescent sensor as well as intensity-based fluorescence sensor.

Capitalizing on GCaMPGLuc and GLucGCaMP working as both BRET and single fluorescence based Ca^{2+} indicators, our approach offered a novel noninvasive GECIs, which integrates ratiometric and single wavelength Ca^{2+} measurements by preserving

externally excitable GCaMP6s where desired, while at the same time providing the bioluminescence of sbGLuc to excite GCaMP6s intramolecularly, thus allowing flexible monitoring of intracellular Ca^{2+} over a range of spatial and temporal scales both *in vivo* and *in vitro*.

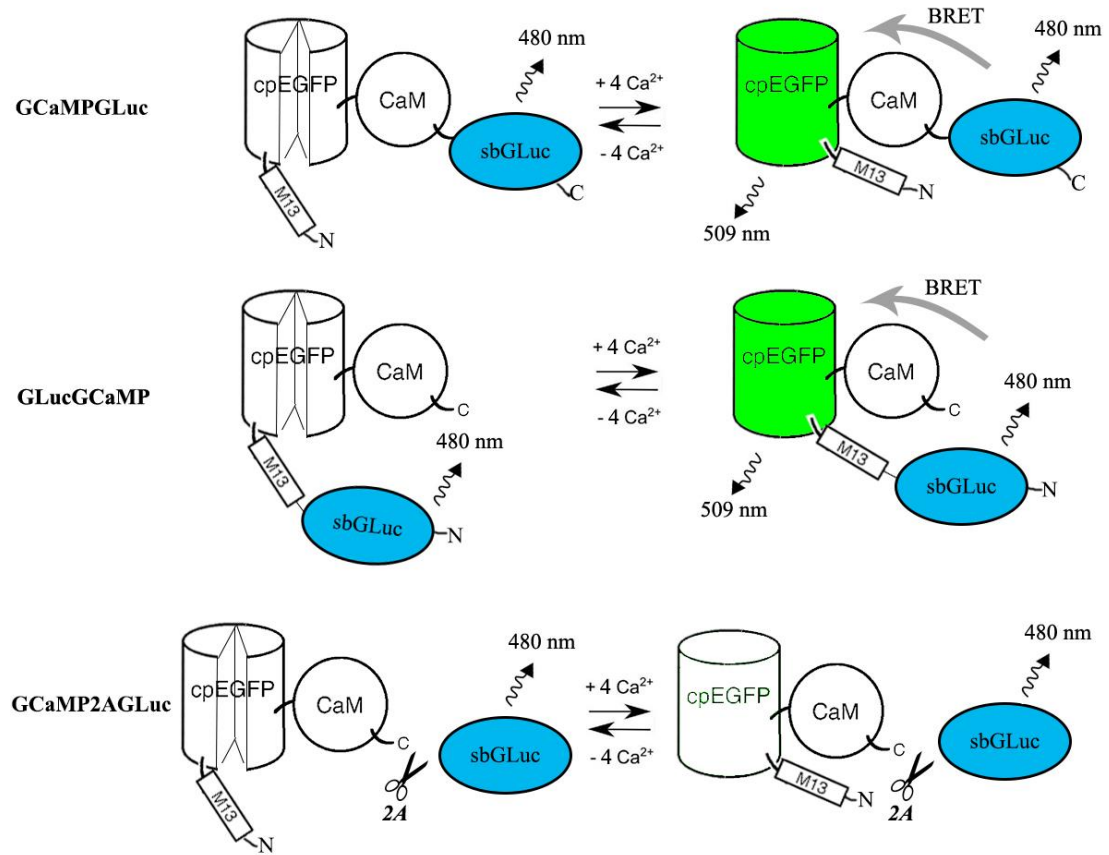


Figure 3-1 Schematic representation of sbGLuc and GCaMP6s based Ca^{2+} indicators and corresponding 2A negative control. Both GCaMPGLuc and GLucGCaMP are fusion proteins of GCaMP6s and sbGLuc/ Δ SS, which interchanges their fusion order. GCaMP6s consists of the M13 fragment from myosin light chain kinase (M13), a circularly permuted EGFP (cpEGFP) and calmodulin (CaM) located N to C terminally. When binding with Ca^{2+} , conformational change triggered by M13 and CaM proximity will form closed and functional EGFP that can be excited by sbGLuc through bioluminescence resonance energy transfer (BRET). Self-cleaving 2A sequence in GCaMP2AGLuc will disconnect GCaMP6s and sbGLuc/ Δ SS, and BRET will be disturbed.

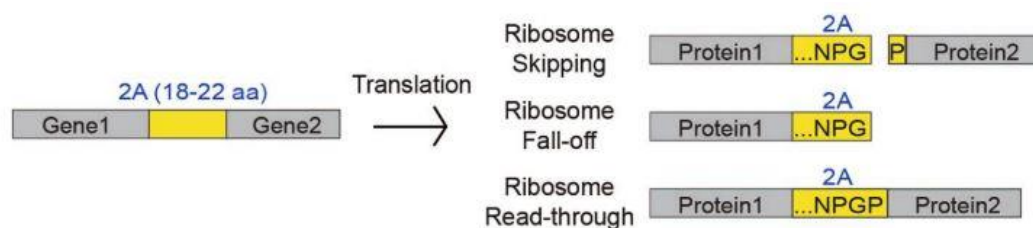


Figure 3-2 Schematic representation of the mechanism of “self-cleaving” 2A peptides. When the ribosome encounters a 2A sequence, a “ribosomal -skip” or “STOP&GO” occurs and a first polypeptide is released while translation of the messenger RNA (mRNA) continues. (Liu et al., 2017).

3.2 Methodology

3.2.1 Plasmid Design

All the restriction enzymes used below are bought from New England Biolabs, USA, unless specified. First, “slow-burn” variant of *Gaussia* luciferase (sbGLuc, mutated at M43L and M110L) was partially subcloned into pcDNA3.1(+) mammalian expression vector, where the secretion signal of the sbGLuc was removed during subcloning. The subsequent vector was named as pcDNA3.1-CAG-sbGLuc/ Δ SS, and its expressed protein refers as sbGLuc. This plasmid was already made before this study.

pGP-CMV-GCaMP6s was obtained from Addgene (Plasmid #40753), and its expressed protein refers as GCaMP6s. GCaMP6s from the pGP vector was PCR amplified with the forward primer “TATGGCTAGCATGACTGGT” and the reverse primer “CGCGGCCGCAAGCTTCGCTGTCAT” and cut with *BmtI*-HF and *HindIII*-HF to create *BmtI* site with 3’ overhang and *HindIII* site with 5’ overhang. pcDNA3.1-CAG-sbGLuc/ Δ SS was then cut by *BmtI*-HF and *HindIII*-HF, and annealed with the GCaMP6s PCR amplified insert, where GCaMP6s located at the N terminal of sbGLuc/ Δ SS with one leucine as a linker. The subsequent vector was named as pcDNA3.1-CAG-GCaMP6s-sbGLuc/ Δ SS, and its expressed protein refers as GCaMPGLuc.

pcDNA3.1-CAG-sbGLuc/ Δ SS was also cut by *NotI*-HF, so did the PCR amplified GCaMP6s insert with the forward primer “GGCCGCGGTCGACTCATC” and the reverse primer “CGCGGCCGCAAGCTTCGCTGTCAT”. Then, the GCaMP6s insert was annealed with the nick of *NotI* site on pcDNA3.1-CAG-sbGLuc/ Δ SS, where

GCaMP6s located at the C terminal of sbGLuc/ Δ SS with 3 alanine as a linker. The subsequent vector was named as pcDNA3.1-CAG-sbGLuc/ Δ SS-GCaMP6s, and its expressed protein refers as GLucGCaMP.

Finally, T2A “self-cleaving” peptide sequence was inserting between GCaMP6s and sbGLuc/ Δ SS in pcDNA3.1-CAG-GCaMP6s-sbGLuc/ Δ SS by QuikChange II Site-Directed Mutagenesis Kit (Agilent, USA). Specifically, the forward primer “AGCTCGAGGGCCGCGGCTCCCTGCTGACCTGCGGCGACG-TGGAGGAGAACCCCGGGCCCA” and its complementary reverse primer were used to amplify unmethylated PCR products containing the T2A insert, and the methylated parental template plasmids were destroyed by *DpnI* following the manufacturer’s instructions. The subsequent vector was named as pcDNA3.1-CAG-GCaMP6s-2A-sbGLuc/ Δ SS, and its expressed protein refers as GCaMP2AGLuc. The completed amino acid sequences of each plasmid product are shown in Figure 3-3.

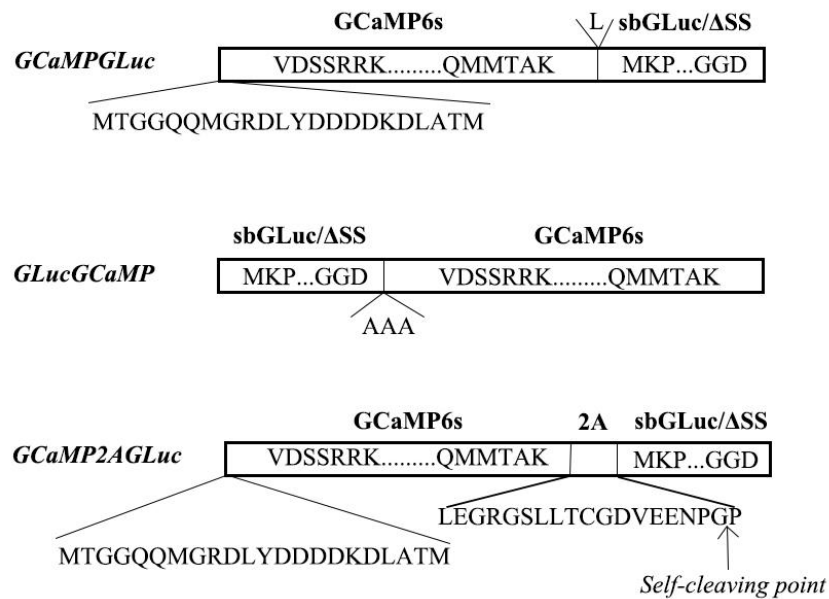


Figure 3-3 Simplified amino acid sequences of GCaMPGLuc, GLucGCaMP and GCaMP2AGLuc. Specifically, 2A in GCaMP2AGLuc is T2A peptide.

3.2.2 Bioluminescent Intracellular Ca^{2+} Response in HEK293 Cells

HEK293 cells were maintained in Dulbecco’s Modified Eagle Medium, high glucose with phenol red (DMEM, Sigma) and supplemented with 10% (V/V) fetal bovine serum (Atlanta Biologicals, USA) and 1% (V/V) penicillin-streptomycin (P/S, Sigma)

under 37 °C and 5% CO₂. Cells were plated in a 96-well white plate with clear flat bottom (ref# 655098, Greiner Bio-One), and the cell culture medium was changed with high Glucose DMEM (10% FBS, 1% P/S) without phenol red (Sigma). When desired cell confluency was reached, except for H row, every three columns were transfected with GCaMPGLuc, GLucGCaMP, GCaMP2AGLuc, and sbGLuc using Lipofectamine 2000 (Invitrogen) following the manufacturer's instructions in a manner of Figure 3-4. After incubating 24 hr, the medium was aspirated carefully and replace with the volume of EGTA and 39 μ M Ca-EGTA buffer (pH 7.20, K_d^{EGTA} =150.5 nM under 20°C in 0.1 M KCl, Biotium, USA) as represented in figure 3-4. Both EGTA and 39 μ M Ca-EGTA buffer was diluted with 20 μ M coelenterazine (NanoLight, USA), 10 μ M ionomycin, and 4 mg/L nigericin (Petr & Wurster, 1997) (Sigma, USA) before use. After equilibrium for at least 5 min, the intracellular free [Ca²⁺] should be 39, 1.35, 0.351, 0.226, 0.150, 0.0376, 0.0167, 0.150 μ M from row A to row H. The white plate was then read for relative luminescence intensity (RLU) in the plate reader (FLUO star OPTIMA, BMG Labtech, Germany) through three channels. One channel is through 485/12 nm (center wavelength/full width at half maximum) filter to measure RLU of sbGLuc emission, the other is through 520/10 nm filter to measure RLU of cpEGFP emission, and the last one is through a lens without any filter to measure RLU of total emission.

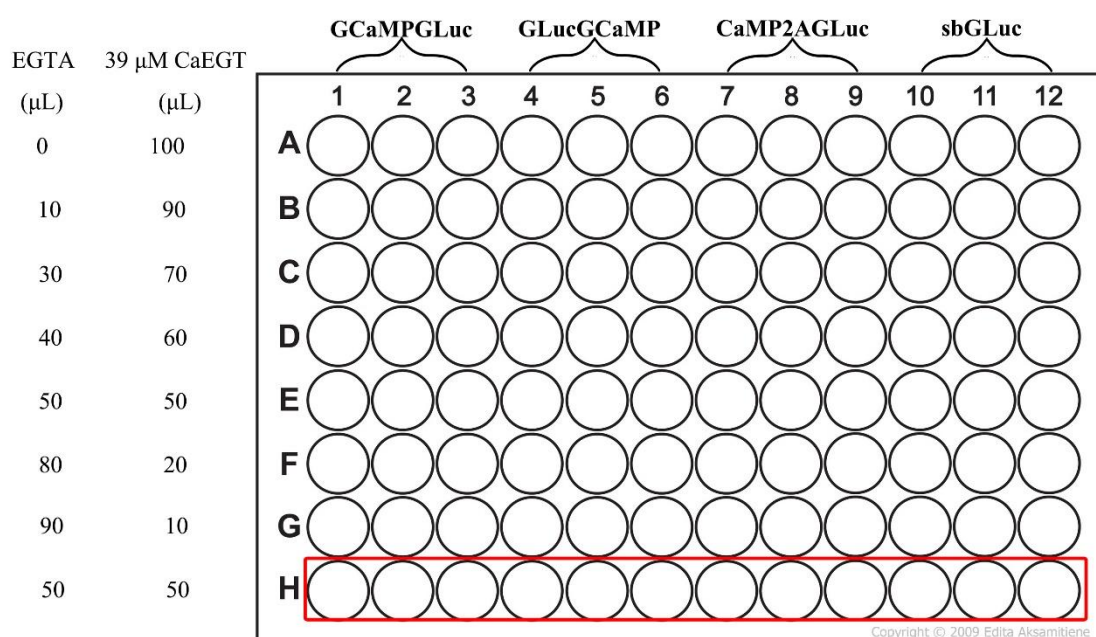
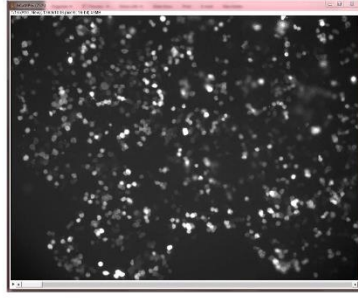


Figure 3-4 Plate arrangement of transfection and free Ca²⁺ calibration. The top of the plate shows the arrangement of plasmid transfection. Each plasmid transfected with

three adjacent columns, except for the H row without any transfection as a control group. The left of the plate shows the volume of EGTA and 39 μ M CaEGTA buffer that was added into each well in the same row.

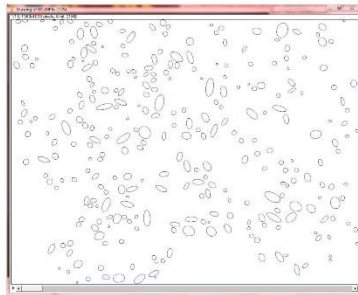
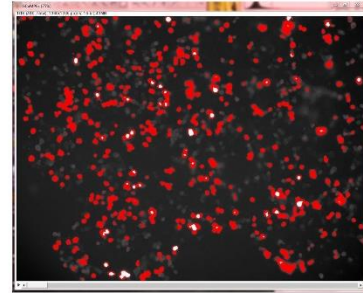
3.2.3 Fluorescent Intracellular Ca^{2+} Response in HEK293 Cells

HEK293 cells were maintained the same as mentioned in section 3-2. The cells were then plated in a 96-well black plate with clear flat bottom (ref# 4680, Corning), and the cell culture medium was changed with high glucose DMEM (10% FBS, 1% P/S) without phenol red. When desired cell confluency was reached, except for the H row, every three adjacent columns were transfected with GCaMPGLuc, GLucGCaMP, GCaMP2AGLuc, and GCaMP6s. The well arrangement was similar to the white plate in Figure 3-4 except for switching sbGLuc to GCaMP6s. After incubating 24 hrs, the medium was aspirated carefully and replaced with the volume of EGTA and 39 μ M Ca-EGTA buffer (pH 7.20, Biotium, USA) as represented in Figure 3-4. Both EGTA and 39 μ M Ca-EGTA buffer was diluted with 10 μ M ionomycin, and 4 mg/L nigericin (Petr & Wurster, 1997) before use. After equilibrium for at least 5 min, the intracellular free $[\text{Ca}^{2+}]$ should be 39.0, 1.35, 0.351, 0.226, 0.150, 0.0376, 0.0167, 0.150 μ M from row A to row H. Then, fluorescent imaging of each well was performed using a Leica DM IRE2 inverted microscope (Leica, Germany) equipped with a Leica CTR MIC controller and a RetigaEX camera (QImaging, Canada). The objective was a $\times 10$ lens (Leica HC PL Fluostar P/N 513852). Images were collected at 20 MHz (1360 x 1036 pixels, 16 bit), 1 second exposure time, 4 signal gains, and 0 offset (SimplePCI imaging software). Excitation filter is a 470/40 nm bandpass filter followed by 500 nm dichroic filter, and emission filter is a 525/50 nm bandpass filter.



1. Raw Image Import to ImageJ.
2. ROI1: Set threshold to exclude background and saturated pixels (white area).
3. ROI2: Randomly draw 4 circles w/o cells as background.

4. Measure the average grayscale of ROI1 and ROI2 as RFU.
5. Extract the results of ROI1 by ROI2.



6. Analyze ROI1 to obtain cell numbers
7. Calculate standard deviation and SEM of RFU based on the obtained cell numbers

Figure 3-5 Workflow of the image analysis.

Raw images transfected by the same plasmid (*e.g.* images of cells expressing GCaMPGLuc in the black plate) were imported into ImageJ as stacks (for details see <https://imagej.nih.gov/ij/docs/index.html>) to group analysis average RFU based on total cells in the field (Figure 3-5). First, I chose an appropriate threshold setting so that most cells in each image has been properly selected as region of interest (ROI) and background has been avoided. Second, average RFU of ROI in each image in stacks was measured, and it's worth to note that calculated RFU here is actually grayscale of ROI in 16 bit which ranges from 0 to 65535, so it is important to avoid choosing saturated pixels as ROI in the first step since they are overexposed. Third, by using particle analysis (Size (pixel²): 40-2000; Circularity: 0.00-1.00; Show: ellipses; check the boxes of Clear results, Include holes, and Summarize), total cell numbers and their standard deviation (SD) in ROI of each image was calculated. Fourth, reset the ROI, randomly chose 3 or 4 small circles from background (no cells) as new ROI in each image, and measured average RFU of the ROI in each image as

background signal. Finally, the background signal was subtracted from the average RFU obtained in the second step, and standard error of the mean (SEM) was calculated using the total cell numbers and their standard deviation from the third step. Since there are three replicates with the same transfected plasmid and free intracellular $[Ca^{2+}]$ in the black plate (see Figure 3-4), chose the calculated result of one image within three replicates to plot Figure 3-8 so that its value fits sigmoidal curve best.

3.3 Results and Discussion

3.3.1 Structure-based Design of the Ca^{2+} Indicators

We designed two genetically encoded Ca^{2+} indicators (GECIs), GCaMPGLuc and GLucGCaMP. Both of them contain a single fluorophore-based GECI GCaMP6s (Chen, 2013), and a “slow-burn” mutated *Gaussia* luciferase (sbGLuc) (Welsh et al., 2009). As showed in Figure 3-1, GCaMPGLuc is a fusion protein of GCaMP6s and sbGLuc/ Δ SS located N to C terminally, whereas GLucGCaMP switches the position such that GCaMP6s located after C terminal of sbGLuc/ Δ SS.

Because bioluminescent resonance energy transfer (BRET) obeys similar rules as Förster resonance energy transfer (FRET), the distance between donor and acceptor should within Förster distances for efficient energy transfer, which is typically 20-80 Å (see section 2.3.2). Based on the very similar crystal structure of GCaMP6m (another variant of GCaMP6 with K78H, M378G, K379S mutation compared to GCaMP6s), the distances from N and C terminus of GCaMP6s fused to sbGLuc to the fluorophore of cpEGFP are around 30 and 50 Å, respectively. Hence, the structure-based designs of GCaMPGLuc and GLucGCaMP satisfied the proximity requirement between donors and acceptors which is required for the efficient BRET.

When free Ca^{2+} binds to CaM of GCaMP6s part, conformational changes due to the Ca^{2+} -CaM-M13 interaction induce a subsequent conformational change in cpEGFP, so that the fluorescence intensity excited by sbGLuc changes. Specifically, at low Ca^{2+} level, the barrel structure of cpEGFP is disrupted by M13 and CaM that fused at its two termini. Ca^{2+} binding on CaM will recruit its binding patternner M13, hence form closed and functional EGFP, which is then excited by sbGLuc emission. Thus, the ratio of cpEGFP emission and sbGluc emission can be used as an indicator of

[Ca²⁺]. Meanwhile, our fusion design does not disturb the original function of GCaMP6s part, and it can still be used as a fluorescence Ca²⁺ indicator alone.

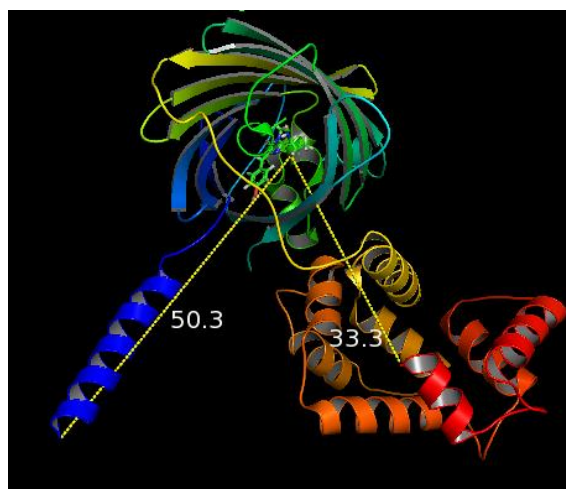


Figure 3-6 Crystal structure of GCaMP6m from the top view (Ding, Luo, Hu, Wang, & Shao, 2014). The rainbow color of the structural diagram indicates the N terminal (in red) to C terminal (in blue). The four bounded Ca²⁺ is colored in green sphere. The distances (yellow dash line) were measured from the α -carbon of the terminal amino acid to the oxygen of aliphatic hydroxyl group on the cpEGFP fluorophore (processed in PyMOL).

3.3.2 Intracellular Ca²⁺ Response in HEK293 Cells

We tested our indicators in HEK293 cells for intracellular Ca²⁺ response. When supplied with CTZ, our BRET-based indicators exhibited excellent Ca²⁺ dependency. Figure 3-7A shows the emission ratio of the GCaMP6s moiety (EM 520 nm) versus the sbGLuc moiety (EM 485 nm), which depends on BRET between GCaMP6s and sbGLuc, when supplied with EGTA-CaEGTA gradient buffer and CTZ. The degree of BRET efficiency is regulated by conformational change induced by Ca²⁺ binding in the GCaMP6s moiety and by the distance and orientation between sbGLuc (donor) and GCaMP6s (acceptor). CaM will recruit M13 after binding with Ca²⁺, and this will lead to close and functional conformation of cpEGFP, which can be excited by sbGLuc emission light. When “self-cleaving” peptide sequence 2A was inserted between GCaMP6s and sbGLuc in GCaMP2AGLuc, BRET between sbGLuc and cpEGFP was interrupted, and it is acting the same as sbGLuc alone, which is not Ca²⁺ dependent. The emission ratio of GCaMPGLuc and GLucGCaMP were normalized and least square-fitted with the Hill equation as shown in Figure 3-7B. Given such calibration data, the [Ca²⁺] in an unknown intracellular environment expressed with

the GECIs can be deduced from the sigmoidal curve of the ratio- $[Ca^{2+}]$ response. An explicit formula for this calibration is derived under 2.1.1 Ca^{2+} Affinities.

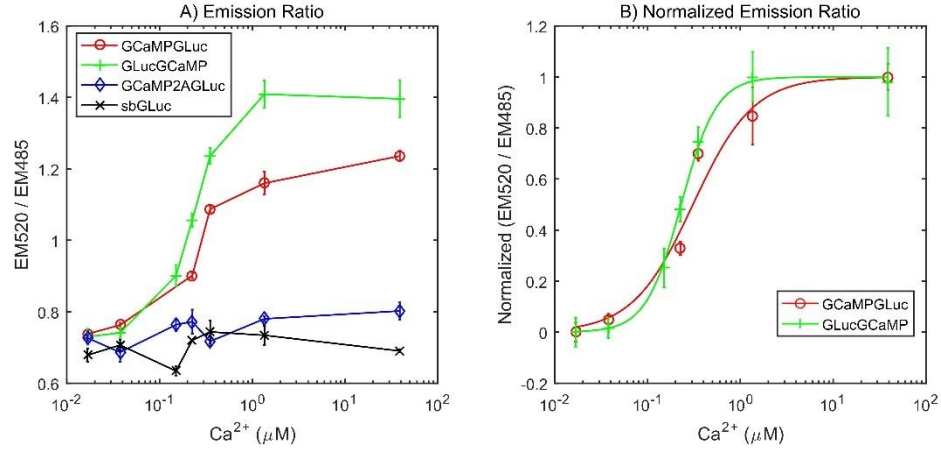


Figure 3-7 *In vitro* Ca^{2+} titration by BRET. A) Emission ratio of 520 nm over 485 nm at different $[Ca^{2+}]$. B) Normalized emission ratio by $(R - R_{min}) / (R_{max} - R_{min})$, where R is the ratio in A), then fitted with the Hill equation. Error bars represent SEM, and $n = 3$.

Figure 3-8 illustrates BRET process during Ca^{2+} binding. When $[Ca^{2+}]$ is increased, the induced conformational changes in cpEGFP of the GCaMP6s moiety of GCaMPGLuc and GLucGCaMP enable more emission light from sbGLuc to be transferred to excite the cpEGFP moiety, whereas neither GCaMP2AGLuc nor sbGLuc can exhibit such energy transfer. As seen in Figure 3-8, with increasing $[Ca^{2+}]$, the ratio of donor sbGLuc emission of 485 nm in GCaMPGLuc and GLucGCaMP is decreasing, while the ratio of acceptor cpEGFP emission of 520 nm in GCaMPGLuc and GLucGCaMP is increasing. The range of $[Ca^{2+}]$ where this intramolecular energy transfer happened are also the same as Figure 3-7. The emission ratio of GCaMP2AGLuc and sbGLuc was relatively stable and unrelated with the changes of $[Ca^{2+}]$. 2A amino acid sequence of GCaMP2AGLuc caused ribosome skipping during translation, and sbGLuc and GCaMP6s was separate, preventing BRET from occurring. Hence, GCaMPGLuc and GLucGCaMP are indeed functioning by BRET mechanism.

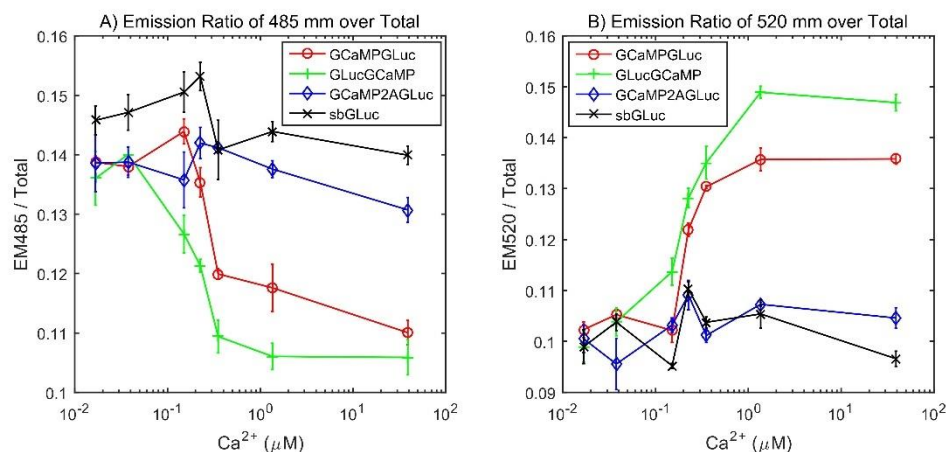


Figure 3-8 Donor-acceptor energy transfer. A) Emission ratio of 485 nm over total light through a clear lens. B) Emission ratio of 520 nm over total light through a clear lens.

Figure 3-9A reveals that when excited solely by the external light, the GCaMP6s part of GCaMPGLuc, GLucGCaMP, and GCaMP2AGLuc acted similar as GCaMP6s alone as Ca^{2+} indicators. The fluorescence was weak at low $[\text{Ca}^{2+}]$, and gradually increased until saturation due to conformational change in M13-cpEGFP-CaM triggered by Ca^{2+} binding. Figure 3-9B showed the normalized fluorescence intensity, which was then fitted with the Hill equation. However, we need to point out that the overall signal intensity of RFU is not as strong as bioluminescence signal, and the background signal from auto-fluorescence is much worse especially in GCaMPGLuc and GCaMP2AGLuc. This, on the other hand, proved the advantage that ratiometric based BRET GECIs do not impair by the same systematic errors that affecting both wavelengths such as CTZ concentration, cell numbers, transfection efficiency, expression level, optical path length and absolute sensitivity of the instrument, because they will be cancelled out in the ratio results. Still, we showed that the GCaMP6s moiety in GCaMPGLuc and GLucGCaMP can function by itself as a fluorescent Ca^{2+} indicator.

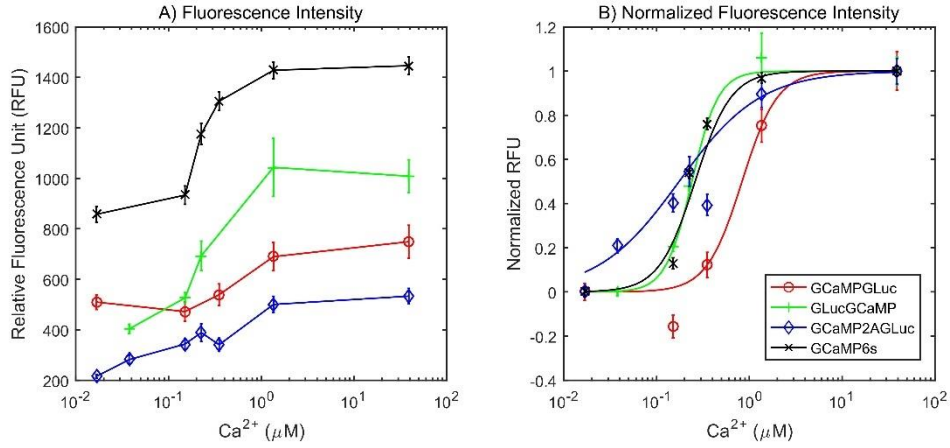


Figure 3-9 *In vitro* Ca^{2+} titration by fluorescence. A) Fluorescence intensity response excited by the external light source. Legend is the same as B). B) Normalized fluorescence intensity response by $(F - F_{\min})/(F_{\max} - F_{\min})$, where F is the RFU, then fitted with the Hill equation (continuous lines). Error bars represent SEM.

In Table 3, we summarized dynamic range, apparent K_d , effective K_d , and Hill coefficient of the Ca^{2+} indicators we used in this study and compared them with previously published Ca^{2+} titration experiments using the purified GCaMP6s. The effective K_d is only applicable to the ratiometric GECIs (*i.e.*, BRET based GCaMPGLuc and GLucGCaMP) and corrected by 485 nm emission intensity ($\lambda_2 = 485$ nm in the relation (5) from 2.1.1 Ca^{2+} Affinities) to make them comparable with the apparent K_d of single wavelength based GCaMP6s. The detailed discussion about the difference between apparent K_d and effective K_d is under 2.1.1 Ca^{2+} Affinities. Back to Table 3, the apparent K_d of BRET based GLucGCaMP is 84% bigger than the apparent K_d of BRET based GCaMPGLuc, whereas such difference is reduced to 26% in comparing the effective K_d where the systematic bias from 485 nm on K_d was eliminated. After considering the systematic error of the instrumental measurement, GCaMPGLuc and GLucGCaMP have similar Ca^{2+} affinities. The effective K_d of BRET based GCaMPGLuc is 55% larger than the reported apparent K_d of GCaMP6s, and the effective K_d of BRET based GLucGCaMP is 15% larger than the reported apparent K_d of GCaMP6s. After considering the systematic error of the instrumental measurement, BRET based GCaMPGLuc and GLucGCaMP have similar Ca^{2+} affinities with GCaMP6s, which means fusing sbGLuc on the N or C terminus of GCaMP6s doesn't have remarkable influence on its Ca^{2+} affinities.

When used as fluorescence-based GECIs, the GCaMP6s parts of GCaMPGLuc and GLucGCaMP showed larger difference in apparent K_d than worked by BRET, where

GCaMPGLuc showed much less affinity on Ca^{2+} than GLucGCaMP. This difference might be expanded by our less accurate measurement of RFU, because of the insufficient block of auto-fluorescence background and the risk of excitation light passing through due to close excitation-emission bandwidth. Thus, such difference cannot be the firm evidence that sbGLuc fused to GCaMP6s affects the Ca^{2+} binding property of GCaMP6s. Not surprisingly, the GCaMP6s part of GCaMP2AGLuc displayed similar affinity on Ca^{2+} binding, since the ribosome skipping caused by the inserted T2A sequence generated separate sbGLuc and GCaMP6s.

Intriguingly, it is noticeable that GCaMP6s exhibited different Ca^{2+} binding affinities under purified form than expressed in HEK293 cells, where GCaMP6s in the cell has lower K_d , less Hill coefficient. This means GCaMP6s in the cell binds more tightly with Ca^{2+} , and this binding process is less cooperative than the purified proteins. Such differences are caused by a variety of factors in the living cell, and one important reason could be the competitive binding of M13 with endogenous CaM (M. Mank & Griesbeck, 2008). Also, the dynamic range of GCaMP6s in living cell is heavily reduced compared with the measurement of the purified one. This is most likely caused by heavy auto-fluorescence background from the living cell.

Table 3 Biophysical properties of Ca^{2+} indicators in HEK293 Cells

Indicator Name	Dynamic range* (max/min)	Apparent K_d (nM) /Effective K_d (nM)	Hill coefficient	Mechanism	Reference
GCaMPGLuc	1.68	205.9/223.3	1.34	BRET	This study
GLucGCaMP	1.93	33.9/165.5	2.30	BRET	This study
GCaMP6s part of GCaMPGLuc	1.59	658.2	2.29	Fluorescence	This study
GCaMP6s part of GLucGCaMP	2.59	12.4	3.08	Fluorescence	This study
GCaMP6s part of GCaMP2AGLuc	2.47	177.5	0.99	Fluorescence	This study
GCaMP6s	1.69	47.9	2.25	Fluorescence	This study
GCaMP6s (Purified Protein)	63.2	144	2.90	Fluorescence	Chen, 2013

* Dynamic range is the ratio of maximal measuring signal (ratio or RFU) divided by minimal measuring signal.

* (Continue) Effective K_d is only applicable to the BRET based GECIs, which the calculation are modified to eliminate the systematic bias of apparent K_d from 485 nm emission, see 3.3.3 Evaluation of Performance for detail.

3.3.3 Evaluation of Performance

In the work described here, I developed two $[Ca^{2+}]$ indicators based on BRET between sbGLuc and GCaMP6s. They both exhibited similar affinities and positive cooperative binding with Ca^{2+} . There are two major advantages of our designed indicators compared with the original GCaMP6 series. First, both are BRET-based ratiometric indicators. The original GCaMP6 series are based on total fluorescence change with Ca^{2+} binding condition, and the fluorescence emission may be influenced by a variety of factors, such as transfection efficiency, cell numbers, intensity of excitation light, optical length, *etc.* The uncertainties associated with quantitating single-wavelength fluorescence emission require that GCaMP6 need to be calibrated with Ca^{2+} gradient buffer in situ each time before use (Palmer & Tsien, 2006), which may be burdensome for many *in vivo* studies. Another difficulty of using GCaMP6 is high auto-fluorescence background from living cells, and I faced the same issue when trying to read fluorescence intensity directly from the plate reader (over 90% signal was auto-fluorescence background). These limitations can be overcome through indicating $[Ca^{2+}]$ by the ratio of two independent emission wavelength as in our design, which cancel out the difference of cell numbers, expression level, transfection efficiency, optical path length and absolute sensitivity of the instrument. Hence, the ratiometric based GCaMPGLuc and GLucGCaMP are more robust than single fluorophore based GCaMP6. This has also been proved by our replicate experiment using the same experiment setting performed at several months interval (Figure 3-10). Second, both of GCaMPGLuc and GLucGCaMP can work by either BRET noninvasively with the luciferase substrate CTZ or via fluorescence by exciting the GCaMP6s moiety alone. Some tissue like brain is extremely fragile to optical fiber installation and possible phototoxicity that could impair the measurement accuracy of fluorescence based Ca^{2+} indicators. Hence, our BRET based indicators working on nontoxic CTZ provide wide flexibility on both *in vivo* and *in vitro* studies. However, compared with the purified GCaMP6s, the dynamic range of GCaMPGLuc and GLucGCaMP is greatly diminished. It is not clear if this is caused by absorption of

bioluminescence and auto-fluorescence from living cell components, which could reduce the maximal ratio at saturated $[Ca^{2+}]$. It is also possible that close bandwidth of our filter setting (Emission filter 485/12 for 485 nm donor channel and 520/10 for 520 nm acceptor channel) allows too much excitation light from the donor pass through the 520/10 nm filter to be received as acceptor fluorescence signal, thus the change in the nominator of the ratio (EM 520 nm) is heavily reduced.

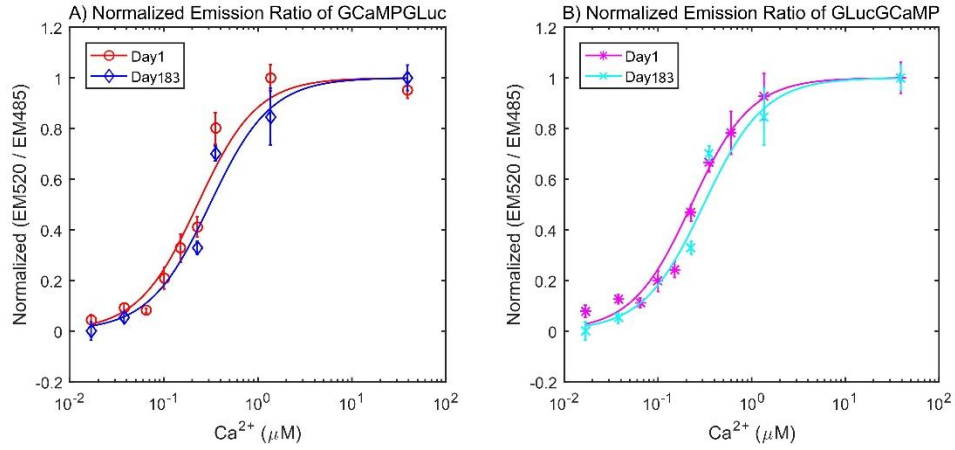


Figure 3-10 Emission ratio of GCaMPGLuc and GLucGCaMP on two dates separated six months exhibits consistent response. Error bars represent SEM, $n = 4$ for day1, and $n = 3$ for day 183.

CHAPTER 4 GOLD NANOPARTICLE ENHANCED BIOLUMINESCENCE

4.1 Introduction

4.1.1 Introduction of luminopsin

Since Au nanoparticles (AuNPs) have great potential to enhance bioluminescence of luciferase by LSPR, this enhancement arises great interest in many luciferase applications including optogenetics. In the broadest sense, optogenetics encompasses a core technology – targetable control tools that respond to light and deliver effector function – and enabling technologies for (i) delivering light into tissues under investigation, (ii) targeting the control tools to cells of interest and (iii) obtaining compatible readouts and performing analysis, such as targeted imaging or electrical recording of evoked activity (Deisseroth, 2011). Luminopsins are one group of optogenetic probes that are fusion proteins of luciferase and opsins, which leverage bioluminescence of luciferase with its substrate to activate opsin to control certain cell activities. Berglund et al. (2016) in our lab reported LMO3, a luminopsin based on *Volvox* channelrhodopsin1 (VChR1) and “slow burn” mutant of *Gaussia* luciferase (sbGLuc). LMO3 is a fusion protein that sbGLuc, VChR1 and EYFP were fused N to C terminally (Figure 5-2, GLucG(LMO) without Kir2.1 trafficking signal). sbGLuc is a “slow-burn” mutant of native GLuc, which has been shown with increased light intensity and delayed emission half-life (Welsh et al., 2009). VChR1 is an algal light-gated cation channel, which is composed of a seven-transmembrane helix domain with the all-*trans*-retinal chromophore and a C-terminal tail of unknown function (Ernst et al., 2008). EYFP at the C terminus of VChR1 allows identification of transfected cells. When expressed in cells, the native secretion signal at the N terminus of sbGLuc will be located outside of the cell membrane and tethered to the membrane domain VChR1, whereas EYFP at C terminus of VChR1 will stay inside the cell membrane (Figure 4-2). LMO3 has showed to generate subthreshold depolarizations upon application of coelenterazine (CTZ), the substrate of GLuc, and activate neurons *in vitro* and *in vivo* (Berglund et al., 2016). However, the emission of sbGLuc is still not bright enough to fully activate VChR1 compared with a physical light source at saturating intensity. To address this problem, on the one hand, a Kir2.1

trafficking signal was inserted between VChR1 and EYFP to improve the surface expression in neurons, and the subsequent probes was names as enhanced LMO3 (eLMO3)(Zhang, Tung, Gross, & Berglund, (In preparation)); on the other hand, it is desirable to enhance the emission light of sbGLuc. Hence, to solve this problem, I proposed a simple strategy that hexahistidine tag (his-tag) was inserted in eLMO3 and conjugated with Ni-NTA-Au nanoparticle to enhance bioluminescence of sbGLuc.

4.1.2 Ni-NTA-Au conjugation with histidine

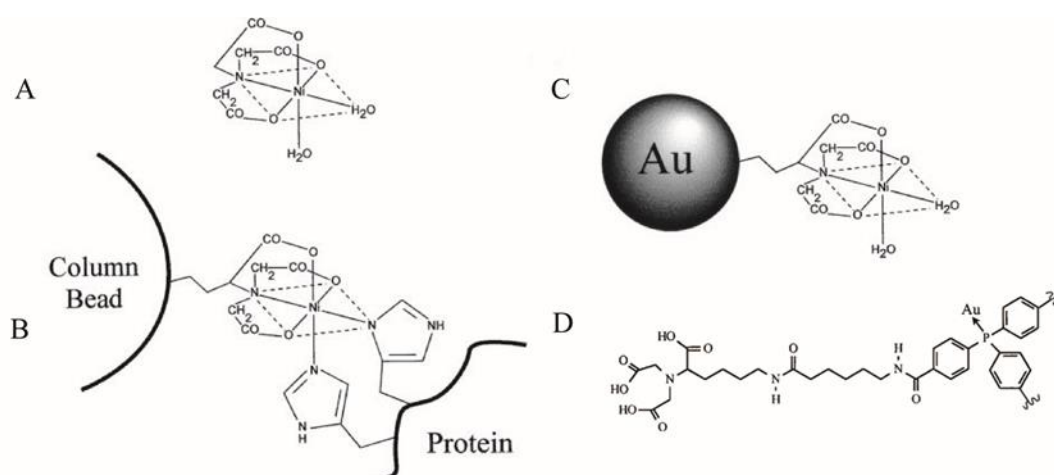


Figure 4-1 Schematic representation of Ni-NTA-Au binding with histidine and its structure. (A) Tetradentate nitrilotriacetic acid (NTA) binds to Ni²⁺ with three carboxyl groups and one nitrogen. (B) Ni-NTA column is one common method to purify his-tagged proteins, of which one Ni-NTA group can bind with two histidine. (C) NTA group can form coordination complex with nanogold. (D) Structure of NTA side chain that coordinate with gold in (C). Each aromatic ring has the same side chain as in (D), which abbreviated as tilde. (Hainfeld et al., 1999)

Ni²⁺ capable of six binding sites can form tetradentate coordination complex with nitrilotriacetic acid (NTA), where three carboxyl groups and one nitrogen of NTA binds to one Ni²⁺ (Figure 4-1A). The leftover two sites of Ni-NTA can bind with two nitrogen of imidazole ring of histidine (Figure 4-1B), and a string of six histidine was found to produce a strong and specific bonding to Ni²⁺ when it was held by NTA. It has made great success in using immobilized Ni-NTA (Ni-NTA column) to purify many proteins with inserted his-tag at their N or C terminus. The dissociation constant (K_d) of his-tagged proteins to Ni-NTA has been measured to be 10⁻¹³ at pH 8 (Schmitt et al., 1993). Such binding is much stronger than most antibody bindings, which typically range from 10⁻⁶ to 10⁻⁹ (Harlow and Lane, 1988). Hainfeld et al. (1999)

synthesized Ni-NTA-Au nanoparticles, of which Ni-NTA was attached to Au surface merely through a 13-carbon chain (Figure 4-1D). Thus, if his-tag was inserted to N or C terminal of sbGLuc, where sbGLuc was tethered outside of cell membrane through VChR1 of eLMO3, AuNP should be able to attach to sbGLuc with great proximity (Figure 4-2), which could enhance bioluminescence through LSPR on AuNP surface.

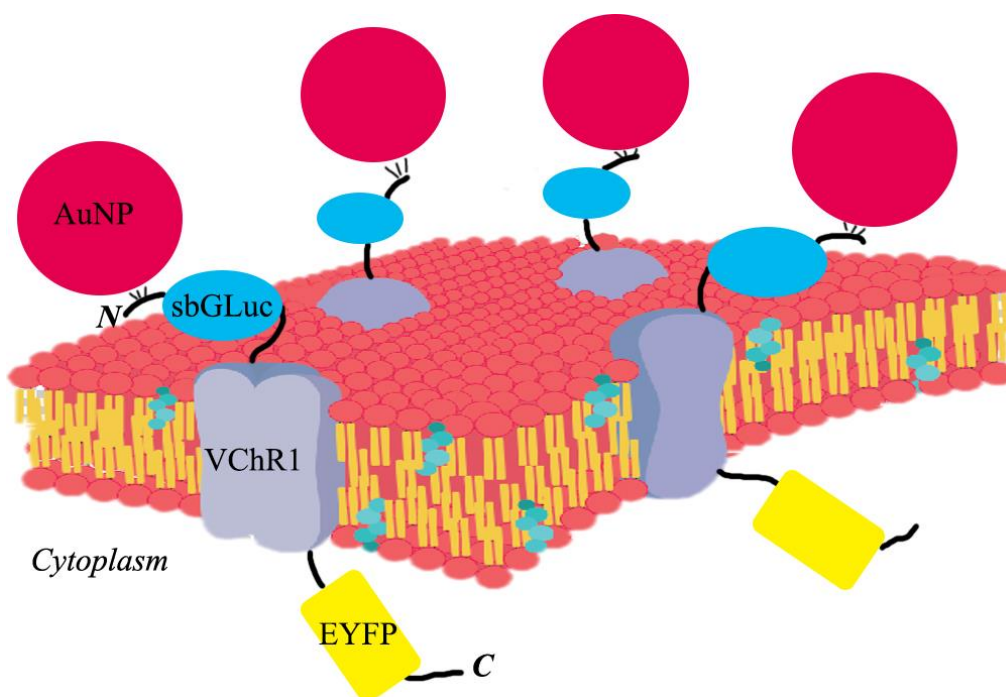


Figure 4-2 Schematic representation of Ni-NTA-Au binding with Nhis_GLuc(LMO). VChR1 is a transmembrane protein, of which extracellular N terminal end fused with sbGLuc, and intracellular C terminal end fused with EYFP as a reporter gene. In this case, his-tag was inserted at the N terminal of sbGLuc, which can conjugate with Ni-NTA-Au. The other two version of his-tagged GLuc(LMO) should bind with Ni-NTA-Au in the same way.

4.2 Methodology

4.2.1 Plasmid Design

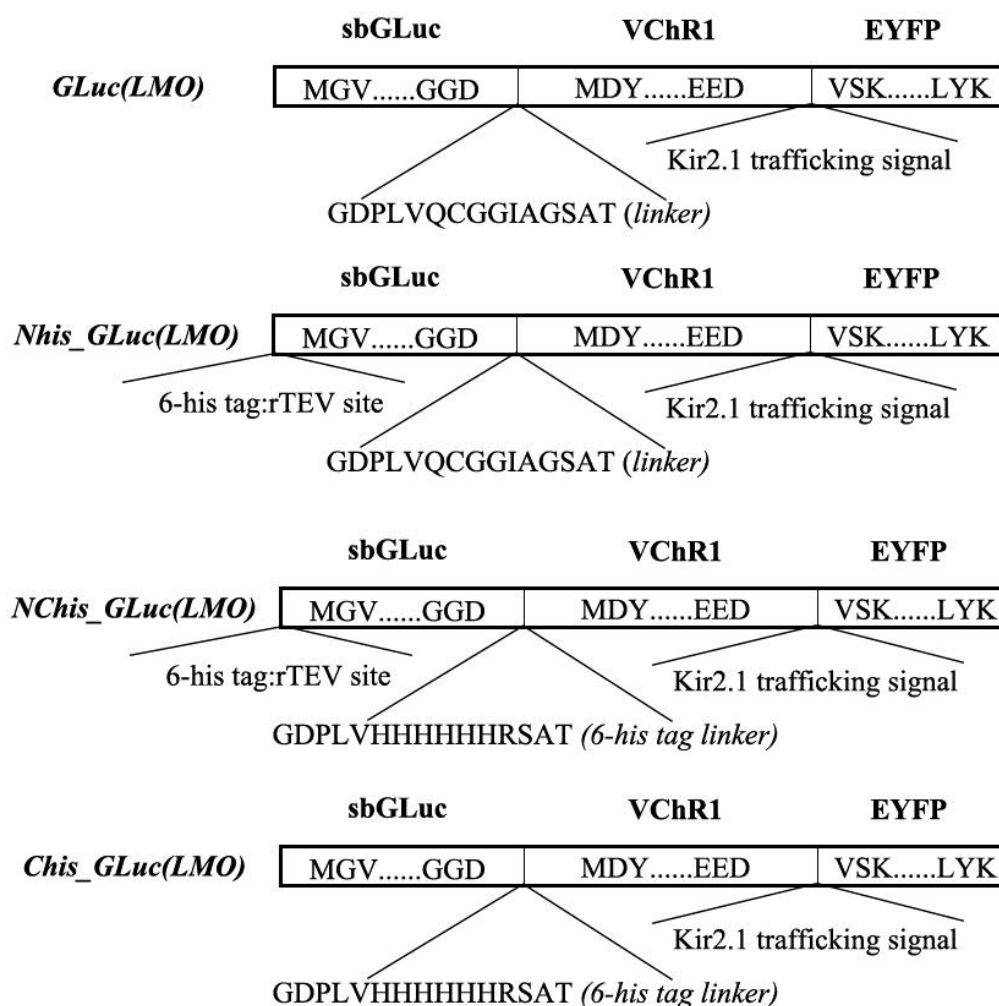


Figure 4-3 Schematic sequence structure of the original eLMO3 (GLuc(LMO)) and designed three his-tagged eLMO3. Nhis_GLuc(LMO), where one his-tag tandem with rTEV site was inserted at N terminal of sbGLuc part. NChis_GLuc(LMO), where besides one his-tag at N terminal, another his-tag was inserted into the linker between sbGLuc and VChR1. Chis_GLuc(LMO), where one his-tag was inserted into the linker between sbGLuc and VChR1.

The eLMO3 coding plasmid, pcDNA3.1/sbGLuc-VChR1-EYFP, was already made in our lab's previous work (Zhang et al., (In preparation)). In this study, his-tag tandem with rTEV site (recombinant tobacco etch virus protease recognition site) was first inserted into N terminal of LMO3 by QuikChange II Site-Directed Mutagenesis Kit (Agilent, USA). Then, another his-tag was inserted to the linker of sbGLuc and VChR1 in the same way. Thus, we generated three versions of six his-tagged LMO3

proteins, which have N terminal his-tagged sbGLuc of LMO3, both N and C terminal his-tagged sbGLuc of LMO3, and C terminal his-tagged sbGLuc of LMO3. We named them as Nhis_GLuc(LMO), NChis_GLuc(LMO) and Chis_GLuc(LMO), respectively (Figure 4-3). The forward primers used in QuikChange II kit was shown in Table 4, where its complementary sequences were reverse primer. Since the explicit structure of GLuc is still unknown, we believed such permutation of his-tag could maximize the chance of the exposure of his-tag to Ni-NTA-Au.

Table 4 Primers Used in QuikChange

His-tag Insertion Place	Forward Primer
N terminus of sbGLuc	TCGAGCCACCATGGTGCATCATCACCATCACCATG AGAACCTGTACTTCCAGGGCG
C terminus of sbGLuc	CTAGTCCATCACCACCACCATCACA

4.2.2 *In vitro* AuNP bioluminescence enhancement

HEK293 cells were maintained in Dulbecco's Modified Eagle Medium, high glucose with phenol red (DMEM, sigma) and supplemented with 10% (V/V) fetal bovine serum (Atlanta Biologicals, USA) and 1% (V/V) penicillin-streptomycin (P/S, Sigma) under 37 °C and 5% CO₂. Ni-NTA-Au with diameter of 1.8, 5, and 10 nm, was purchased directly from the company (Nanoprobes, USA), of which the concentration is 10 µM, 500 nM, and 50 nM, respectively. As a control, we also purchased 5 and 10 nm simple gold nanoparticle (simple Au) stabilized in 0.1 mM PBS from the company (Sigma, USA), of which the concentration is 100 and 10 nM, respectively. First, we examined the effect of AuNP size on bioluminescence enhancement. After HEK293 cells were plated into a 96-well white plate with clear flat bottom (ref# 655098, Greiner Bio-One), the cells were transfected with GLuc(LMO), Nhis_GLuc(LMO), NChis_GLuc(LMO), and NC_GLuc(LMO) using lipofection at proper cell confluency. On the next day after the transfection, the medium of the cells expressing each kind of the LMO proteins was replaced with DPBS (Sigma, USA) diluted with 500 pM of one of AuNPs described above (3 sizes of Ni-NTA-Au, 2 sizes of simple Au, and the same volume of 10 nm Ni-NTA-Au buffer), then incubated in the cell incubator (37 °C, 5% CO₂) for 15 mins. Then, the cells were carefully washed by replacing the medium with DPBS once. Finally, DMEM with 15

μ M coelenterazine (NanoLight, USA) was added into each well, and relative luminescence intensity (RLU) of each well was measured by the plate reader (FLUO star OPTIMA, BMG Labtech, Germany). Second, we examined the effect of different concentration of 10 nm AuNP on bioluminescence enhancement. Cells were prepared and transfected in a 96-well white plate as same as the first experiment. On the next day after the transfection, the medium of the cells expressing the different LMO proteins was replaced with DPBS diluted with 0.5, 1, and 5 nM 10 nm Ni-NTA-Au; and 5 nM 10 nm simple Au stabilized in citrate buffer (Sigma, USA). Since we observed in the previous experiment that the 10 nm simple Au stabilized in 0.1 mM PBS will aggregate after diluted in DPBS, here we replaced it with the same size simple Au stabilized in citrate buffer, which is stable in DPBS. After incubating in the CO₂ incubator (37 °C, 5% CO₂) for 15 mins, the cells were carefully washed by replacing the medium with DPBS once. Finally, DMEM with 15 μ M coelenterazine (NanoLight, USA) was added into each well, and relative luminescence intensity (RLU) of each well was measured by the plate reader (FLUO star OPTIMA, BMG Labtech, Germany). The relative luminescence unit (RLU) data were analyzed by using RStudio program.

We also examined the expression of all four versions of the proteins by western blot and fluorescence imaging. For western blot, a new batch of HEK293 cells was plated in a 6-well culture plate (Company) and transfected with the four GLuc(LMO)s as mentioned above. The cells were lysed by adding 1 ml RIPA buffer (Thermo Scientific, USA) in each well by following the manufacturer's instructions. The protein concentration was then determined by Bradford assay (Bio-Rad, USA), and 20 μ g total protein of each sample was run in 4%-6% sodium dodecyl sulfate bis-acrylamide (SDS-PAGE) electrophoresis gel (Bio-Rad, USA). The protein in the gel was subsequently transferred onto a polyvinylidene difluoride (PVDF) membrane (Immobilon-P; Millipore). The blot was incubated in the primary antibody: rabbit polyclonal anti-GFP antibody (Code No: 598; 1:2,000 dilution; MBL International, MA). β -tubulin was used as a positive control to confirm the protein was extracted successfully and to confirm equal protein quantity loading. The secondary antibody was goat anti-rabbit IgG (heavy and light chains) conjugated with a fluorescent dye, Dylight® 680 (1:10,000 dilution; Thermo Scientific, USA). The blotted membrane was imaged by Odyssey scanner (LI-COR, USA). Fluorescence images of the cells used in *in vitro* AuNP incubation were captured by a Leica DM IRE2 inverted

microscope (Leica, Germany) equipped with a Leica CTR MIC controller and a RetigaEX camera (QImaging, Canada). Imaging setup was optimized for individual wells to suit for representation.

4.3 Results and Discussion

4.3.1 Structure of his-tagged GLuc(LMO)

We designed three his-tagged GLuc(LMO) fusion proteins based on luminopsin eLMO3 (Zhang, In preparation), which is mainly composed of sbGLuc, VChR1 and EYFP from N to C terminus (Figure 4-3). His-tag was inserted to the N terminus, C terminus, or both in sbGLuc of eLMO3, which located outside of cell membrane after expression. Since the explicit structure of GLuc is still unknown, such permutation could maximize the chance of the exposure of his-tag to Ni-NTA-Au. It has been shown that Ni-NTA-Au can specifically bind with purified his-tagged adenovirus knob protein *in vitro* (Hainfeld et al., 1999). Meanwhile, Ni-NTA was synthesized with Au surface merely through a 13-carbon chain (Figure 4-1D), thus such proximity between Au surface and sbGLuc could facilitate scattering instead of absorption of bioluminescence (the latter will quench bioluminescence).

4.3.2 *In vitro* Ni-NTA-Au Bioluminescence Enhancement in HEK293 cells

The successful expression of four GLuc(LMO)s were confirmed by both fluorescence imaging (Figure 4-4A) and western blot (Figure 4-4B). The results of western blot showed that NChis_GLuc(LMO) and Chis(LMO) have two band, the lower one is near the calculated size (84.4 kDa), and higher one is about twice bigger (~150 kDa). Crystallography of ChR2 (structurally close related with VChR1) found that ChR2 can form stable dimer in SDS (Muller, Bamann, Bamberg, & Kuhlbrandt, 2011). Thus, the double band implied that VChR1 could also form stable dimer in SDS. Also, compared with the band of unmodified GLuc(LMO), the band of Chis_GLuc(LMO) is thicker than N and NC version of GLuc(LMO). Since the same amount of total protein were loaded when running the western blot, it is certain that the expression levels of the four GLuc(LMO)s are different. Chis_GLuc(LMO) kept the similar expression level as GLuc(LMO), whereas Nhis_GLuc(LMO) and NChis_(LMO) have less expression products. This was also confirmed by microscopic observation of fluorescent HEK cells under the same condition (Figure 4-5). This was probably

caused by the interference of the his-tag (together with rTEV site) on the native secretion signal of sbGLuc, since the secretion signal was located at the N terminal of sbGLuc, which plays a critical role on surface trafficking of LMO (Zhang et al., submitted).

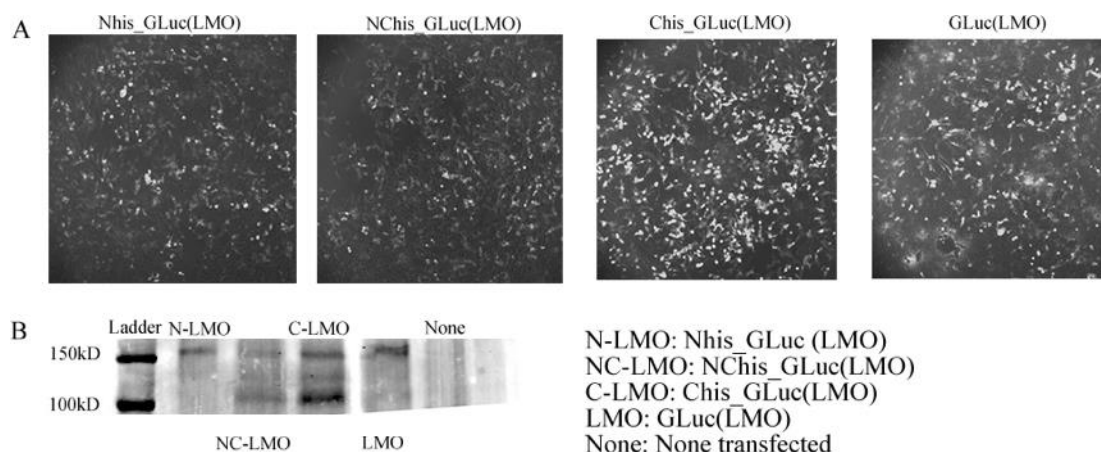


Figure 4-4 Nhis_GLuc(LMO), NChis_GLuc(LMO), Chis_GLuc(LMO) and GLuc(LMO) expression in HEK293 cells. (A) Four GLuc(LMO)s are expressed on the membrane of the cell, of which the fluorescence emitted from the periphery of the cells. (B) Western blot results. The weaker lower band at 100 kDa is the monomeric portion of four GLuc(LMO), and the strong band at 150 kDa is the dimer.

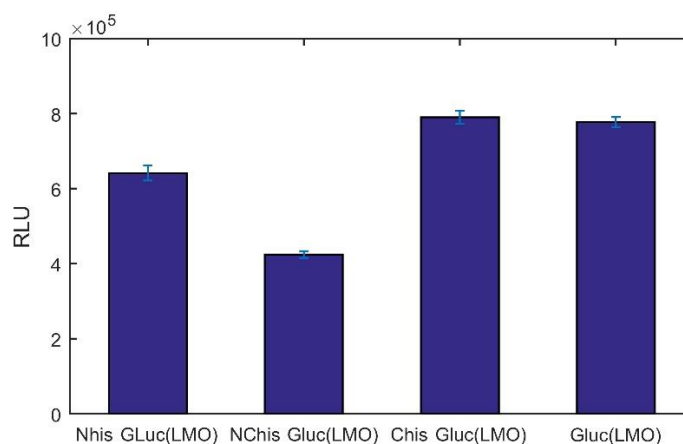


Figure 4-5 Total light yield of the four GLuc(LMO)s. RLU: relative luminescence unit. Error bars represent SEM. $n = 8$.

Next, we investigated the AuNP size effect of both Ni-NTA-Au and simple Au on bioluminescence of four GLuc(LMO)s. Figure 4-6 showed the enhancement factor, which is the ratio of RLU incubated with AuNPs over RLU without AuNPs of the same plasmids, increased with escalating sizes of AuNPs for both Ni-NTA-Au and simple Au under the same concentration 0.5 nM. However, under the current

concentration, all three sizes of Ni-NTA-Au have negative effect (enhancement factor <1) on bioluminescence, whereas simple Au has bigger enhancement factor compared with the same sizes of Ni-NTA-Au, and 10 nm simple Au exhibited up to 15% increase of bioluminescence in NChis_GLuc(LMO) version or no decrease at least for the rest plasmids. This suggested that under current concentration, Ni-NTA coated AuNPs absorb more than scatter the lights from the luciferase, and simple Au without Ni-NTA have less such side effect, while increasing the size of AuNPs can reduce the unwanted absorption of the luciferase emission. Noticeably, GLuc(LMO) has similar trends in both Ni-NTA-Au and simple Au with other his-tagged GLuc(LMO)s plasmids. This suggested that simple Au behaves similarly with Ni-NTA-Au in interaction with luciferase and Ni-NTA coating doesn't increase the specificity of Au-luciferase interaction. It is also noticeable that after diluting the simple Au (stabilized in 0.1 mM PBS) into DPBS, the color of the simple Au changed from red to black suggesting the aggregation of Au due to high ionic strength, which was later confirm by the red shift of the absorption peak of the simple Au-DPBS solution (spectrum data not shown). Thus, the simple Au diameter in this experiment might be bigger than 10 nm. Still, the results suggested that increasing the size of AuNPs to 10 nm could potentially enhance bioluminescence instead of quenching the light. This observation was also consistent with the prediction of LSPR theory and experiments that bigger AuNPs size allows the wider absorption across-sections and the higher ratio of scattering to absorption (He, Liu, Kong, & Liu, 2005; Jain et al., 2006; Link & El-Sayed, 1999).

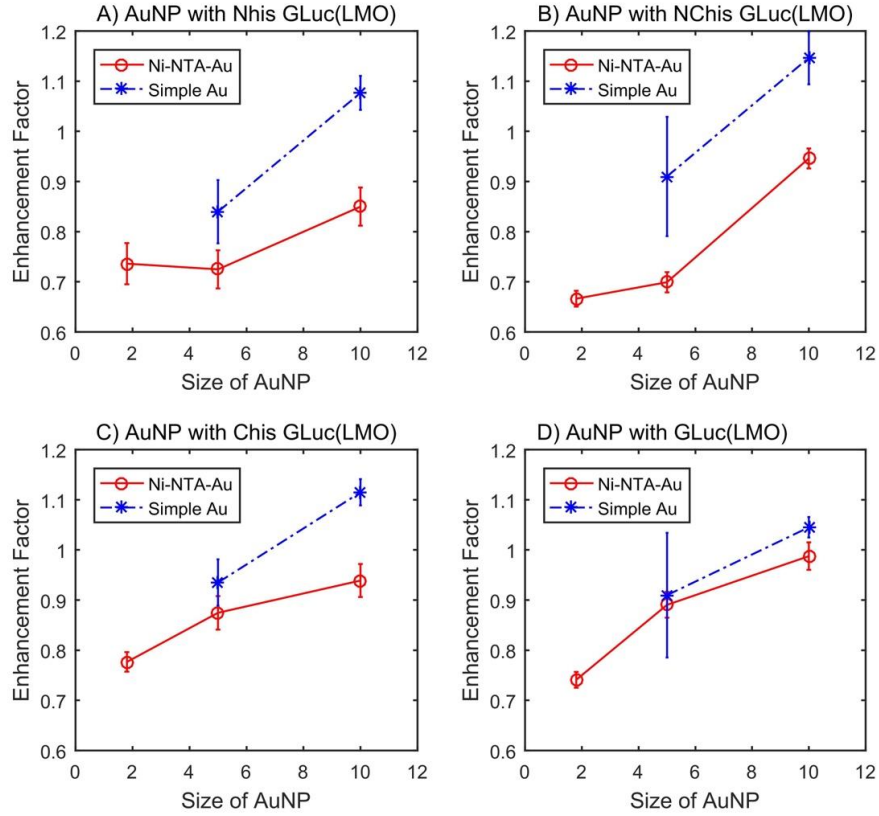


Figure 4-6 Enhancement factor of Nhis_GLuc(LMO), NChis_GLuc(LMO), Chis_GLuc(LMO) and GLuc(LMO), after incubating with 0.5 nM of various size of AuNPs. Enhancement factor = RLU incubated with AuNPs / RLU incubated with buffer only. Error bars represent SEM, and $n = 8$.

Then, I investigated the enhancement effect of 10 nm diameter Ni-NTA-Au with increased concentration (0.5, 1, 5 nM) and 10 nm diameter simple Au with the concentration of 5 nM, which incubated with four GLuc(LMO)s expressed in HEK293 cells. The simple Au used here was stabilized in the citrate buffer instead of 0.1 mM PBS, which does not aggregate after diluted in DMEM confirmed by the absorption spectrum of the simple Au-DPBS solution (data not shown). The RLU of each condition was first normalized based on their corresponding plasmid without Ni-NTA-Au incubation to obtain the enhancement factors, which is the ratio of the RLU versus the mean RLU of the same plasmid without Ni-NTA-Au. A one-way ANOVA was conducted to the RLU at the various concentrations of Ni-NTA-Au. If any significance at the $P < .05$ level was detected, post hoc multi-comparison using Turkey HSD test was followed to indicate between which groups in the same plasmid are significant different at the $P < .05$ level. From Figure 4-7, the RLU of

Nhis_GLuc(LMO) and GLuc(LMO) incubated with 5 nM simple Au ($d = 10$ nm) exhibited 25% and 28% bioluminescence enhancement respectively compared with the same condition without adding AuNPs ($F(4,35) = 4.66$, $*P = 0.004$, $n = 8$ in one-way ANOVA, and $*P = 0.027$ between 0 and 5 nM simple Au in Turkey's HSD test for Nhis_GLuc(LMO); $F(4, 35) = 4.33$, $*P = 0.006$, $n = 8$ in one-way ANOVA, and $*P = 0.003$ between 0 and 5 nM simple Au in Turkey's HSD test for GLuc(LMO)). GLuc(LMO) also showed the elevated enhancement with the increasing concentration of Ni-NTA-Au concentration from 0.5 nM to 5 nM, whereas other his-tagged versions didn't have similar trends. The results also turned out that Ni-NTA-Au with bigger size (10 nm) still cannot significantly enhance the bioluminescence, however, simple Au can significantly enhance the bioluminescence both in his-tagged Nhis_GLuc(LMO) and GLuc(LMO) without his-tag. It could possibly have two explanations: the Ni-NTA-Au doesn't bind to the his-tagged proteins, or specific bound Ni-NTA-Au is not in the wrong position where the distance to the sbGLuc is prone to absorb but not enhance the bioluminescence. Meanwhile, the simple Au can bind with sbGLuc of GLuc(LMO)s through nonspecific binding of available "high Gibbs free energy" surface on AuNPs, since Au can spontaneously form Au-S covalent bonds with 5 cysteine residues in sbGLuc (Ackerson et al., 2006), which enables the LSPR between Au surface and sbGLuc. Abhijith et al. (2014) also showed that simply adding Au-Ag alloy nanoparticles to purified luciferase can enhance bioluminescence, which could be the results of Au-S interaction. Indeed, it is recommended for the further study to take electron microscopic picture of the cells by SEM to see where the AuNPs actually bind. Also, more theoretical analysis should be conducted to determine the optimum distances and sizes of AuNPs to the sbGLuc to obtain higher enhancement.

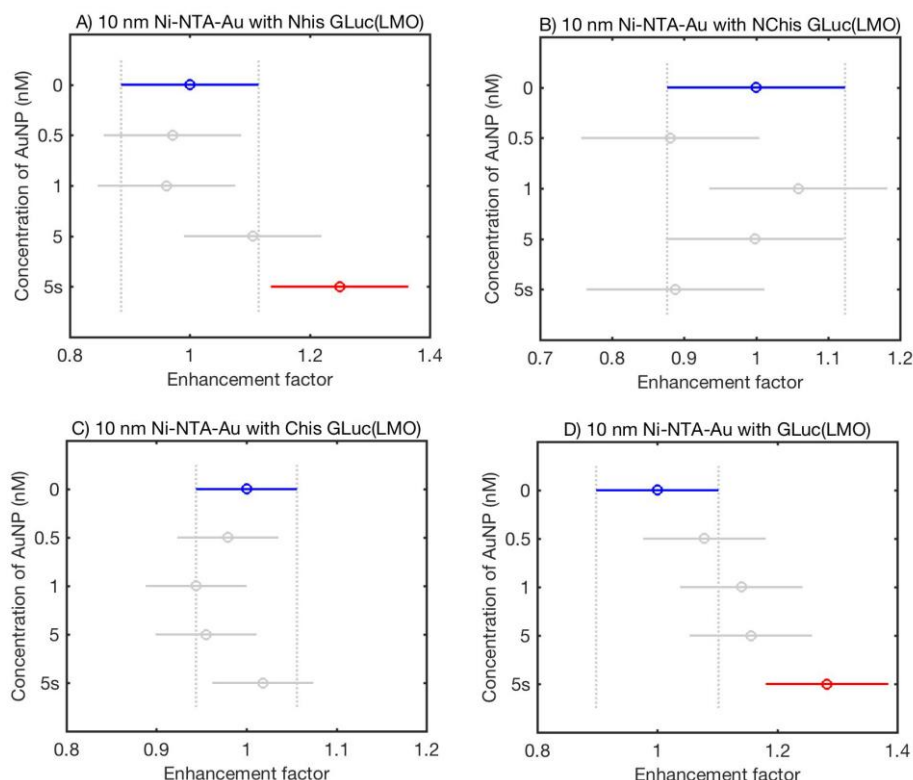


Figure 4-7 Enhancement factors of Nhis_GLuc(LMO), NChis_GLuc(LMO), Chis_GLuc(LMO) and GLuc(LMO), after incubating with 0.5, 1, 5 nM of Ni-NTA-Au and simple Au (both $d = 10$ nm). 5s is the concentration of 5 nM simple Au. Statistical significance was compared with RLU without Ni-NTA-Au (0 nM). Error bars represent SEM, $n = 8$. * $P < 0.05$ by one-way ANOVA and Turkey's HSD test.

4.3.3 Evaluation of the Performance

Here, we proposed a simple strategy of leveraging histidine-Ni-NTA coordination complex and LMO proteins such that AuNP could be conjugated with sbGLuc on the cell membrane and enhance its bioluminescence. However, the results turned out that the Ni-NTA-Au at current sizes and binding position cannot enhance the bioluminescence, whereas plainly adding simple Au to the cell can enhance around 25 to 28% bioluminescence of sbGLuc expressed on the cell membrane, which we thought could be caused by the nonspecific binding of simple Au on sbGLuc through Au-S interaction. Although our Ni-NTA-Au doesn't function as expected, our results are the first to show that AuNPs can directly enhance bioluminescence on the cell surface, which expands the AuNP enhancement on the bioluminescence of some purified luciferase proteins (Abhijith, Sharma, Ranjan, & Thakur, 2014; Du et al., 2014). However, there are still many shortcomings that can be improved for future

study. First, LSPR theoretically enables much stronger enhancement (Zhan, Zhang, Zhao, Liu, & He, 2015). It has already been shown that AuNPs conjugated with purified horseradish peroxidase (HRP) can exhibit near 10-fold enhancement (Du et al., 2014). It is still a challenge to design proper AuNP docking strategy when the native GLuc structure remains unknown. Thus, we believe after the unveiling of GLuc structure, the structure guided design of AuNP conjugation could greatly ameliorate the enhancement efficiency. Second, since AuNP surfaces are intrinsically active, nonspecific binding of AuNPs is another great challenge if it is implemented *in vivo*. Although in our study the simple Au exhibited greater enhancement than Ni-NTA-Au, which I believe is caused by Au interaction with cysteine in sbGLuc, the enhancement by specific binding AuNPs is a major objective to achieve in the future. Currently, some *in vivo* applications of AuNPs will conjugate AuNP with targeted antibodies to reduce nonspecific binding (Montenegro et al., 2013). But, immunoglobulin (IgG) binds with simple Au nonspecifically, and it requires specific epitope fused to the target proteins, which still needs to be tested for its enhancement performance. Third, further studies should be performed to examine whether the enhanced bioluminescence can improve activation of VChR1 in LMO. Due to the limitation of time, this part was not performed in this study, but it will be an important application of this study.

CHAPTER 5 CONCLUSION OF THE THESIS

In the Chapter 3, I designed GCaMPGLuc and GLucGCaMP, which can work either as a bioluminescence resonance energy transfer (BRET)-based ratiometric Ca^{2+} indicator or as a fluorescence-based intensimetric Ca^{2+} indicator. When used as BRET-based Ca^{2+} indicators, binding of free Ca^{2+} on CaM of the GCaMP6s moiety will trigger conformational changes due to the Ca^{2+} -CaM-M13 interaction, and induce a subsequent conformational change in cpEGFP, which ultimately determine the efficiency of BRET between sbGLuc and cpEGFP indicated by the ratio of the EGFP emission peak versus the sbGLuc emission peak. When used as fluorescence based Ca^{2+} indicators, their GCaMP6s part can function separately from sbGLuc and the cpEGFP moiety can be excited directly by external light resources. The two indicators were tested in HEK293 cells and the resulting emission was able to be fitted with the Hill equation to report their dynamic range, apparent K_d , effective K_d (corrected apparent K_d of the ratiometric GECIs to be comparable with the apparent K_d of GCaMP6s) and Hill coefficient. The effective K_d of GCaMPGLuc is 223.3 nM, which is close to the effective K_d of GLucGCaMP 165.5 nM and the apparent K_d of GCaMP6s 144 nM. Thus, fusing sbGLuc to GCaMP6s either N or C terminus doesn't remarkable affect the overall Ca^{2+} affinities of GCaMP6s. The new designs conserve the sensitivity and accuracy of the original GCaMP6 and provide BRET-based ratiometric measurements of $[\text{Ca}^{2+}]$, thereby expanding the ability of GECIs in living cells where noninvasive detection is required. Future studies can test the Ca^{2+} binding kinetics and pK_a of the indicators, improve the dynamic range, and further evaluate their *in vivo* performance.

In Chapter 4, I designed three hexahistidine-tagged GLuc(LMO)s, which could ideally conjugate with Ni-NTA-Au nanoparticles on the cell surface with high specificity. Chis_GLuc(LMO) and GLuc(LMO) have higher expression level in HEK293 cells compared with Nhis_GLuc(LMO) and NChis_GLuc(LMO), suggesting that the insertion of his-tag at the N terminus could interfere with the normal cell processes of the native secretion signal of GLuc. After investigating the size and concentration of various Ni-NTA-Au and comparing with simple Au nanoparticles without Ni-NTA coating, it turned out that Nhis_GLuc(LMO) and GLuc(LMO) without his-tag incubated with 5 nM simple Au of 10 nm diameter

showed 25% and 28% bioluminescence enhancement compared with the same plasmid without adding AuNPs, respectively. However, Ni-NTA-Au failed to exhibit any significant enhancement in all four GLuc(LMO)s. The enhancement from the simple Au could be the results of nonspecific binding between the simple Au surfaces and sulfhydryl groups from 5 cysteines in sbGLuc. Still, this study proved that AuNPs can conjugate with luciferase to leverage LSPR of Au surface to enhance the bioluminescence intensity on the cell surfaces. Thus, AuNPs potentially could be used to improve luciferase dependent biosensors, which benefits from higher bioluminescence intensity. Future studies can improve specificity of AuNP binding such as capping with small molecules with sulfhydryl group to further block the free surface of AuNPs, improve efficient LSPR of AuNP with luciferase, and investigate spectral characteristics of AuNP enhanced bioluminescence and the enhancement effect on VChR1 of LMO.

REFERENCES

- Abhijith, K. S., Sharma, R., Ranjan, R., & Thakur, M. S. (2014). Facile synthesis of gold-silver alloy nanoparticles for application in metal enhanced bioluminescence. *Photochem Photobiol Sci*, 13(7), 986-991. doi:10.1039/c4pp00046c
- Ackerson, C. J., Jadzinsky, P. D., Jensen, G. J., & Kornberg, R. D. (2006). Rigid, Specific, and Discrete Gold Nanoparticle/Antibody Conjugates. *Journal of the American Chemical Society*, 128(8), 2635-2640. doi:10.1021/ja0555668
- Akerboom, J., Calderón, N. C., Tian, L., Wabnig, S., Prigge, M., Tolö, J., . . . Macklin, J. J. (2013). Genetically encoded calcium indicators for multi-color neural activity imaging and combination with optogenetics. *Frontiers in molecular neuroscience*, 6.
- Aslan, K., & Geddes, C. D. (2009). Metal-enhanced chemiluminescence: advanced chemiluminescence concepts for the 21st century. *Chemical Society Reviews*, 38(9), 2556-2564.
- Aubin-Tam, M.-E., & Hamad-Schifferli, K. (2005). Gold nanoparticle– cytochrome c complexes: The effect of nanoparticle ligand charge on protein structure. *Langmuir*, 21(26), 12080-12084.
- Berglund, K., Clissold, K., Li, H. E., Wen, L., Park, S. Y., Gleixner, J., . . . Hochgeschwender, U. (2016). Luminopsins integrate opto- and chemogenetics by using physical and biological light sources for opsin activation. *Proc Natl Acad Sci U S A*, 113(3), E358-367. doi:10.1073/pnas.1510899113
- Berridge, M. J. (1993). Inositol trisphosphate and calcium signalling. *Nature*, 361(6410), 315-325.
- Bewig, K. W., & Zisman, W. A. (1965). The Wetting of Gold and Platinum by Water. *The Journal of Physical Chemistry*, 69(12), 4238-4242. doi:10.1021/j100782a029
- Bornhop, D. J., Szent-Gyorgyi, C., Ballou, B. T., Dagnal, E., Bryan, B., Contag, C. H., & Seavick-Muraca, E. M. (1999). *Cloning and characterization of new bioluminescent proteins*. Paper presented at the Biomedical Imaging: Reporters, Dyes, and Instrumentation.
- Brancolini, G., Kokh, D. B., Calzolari, L., Wade, R. C., & Corni, S. (2012). Docking of ubiquitin to gold nanoparticles. *ACS Nano*, 6(11), 9863-9878. doi:10.1021/nn303444b
- Carafoli, E. (2004). Special issue: calcium signaling and disease. In: Academic Press.
- Chen, T. W., Wardill, T. J., Sun, Y., Pulver, S. R., Renninger, S. L., Baohan, A., . . . Kim, D. S. (2013). Ultrasensitive fluorescent proteins for imaging neuronal activity. *Nature*, 499(7458), 295-300. doi:10.1038/nature12354
- Clapp, A. R., Medintz, I. L., & Mattoussi, H. (2006). Förster Resonance Energy Transfer Investigations Using Quantum-Dot Fluorophores. *ChemPhysChem*, 7(1), 47-57. doi:10.1002/cphc.200500217
- Deisseroth, K. (2011). Optogenetics. *Nat Methods*, 8(1), 26-29. doi:10.1038/nmeth.f.324
- Deng, Z. J., Liang, M., Toth, I., Monteiro, M. J., & Minchin, R. F. (2012). Molecular interaction of poly (acrylic acid) gold nanoparticles with human fibrinogen. *ACS Nano*, 6(10), 8962-8969.

- Ding, J., Luo, A. F., Hu, L., Wang, D., & Shao, F. (2014). Structural basis of the ultrasensitive calcium indicator GCaMP6. *Science China Life Sciences*, 57(3), 269-274. doi:10.1007/s11427-013-4599-5
- Dodd, A. N., Kudla, J., & Sanders, D. (2010). The language of calcium signaling. *Annu Rev Plant Biol*, 61, 593-620. doi:10.1146/annurev-arplant-070109-104628
- Dominguez-Medina, S., McDonough, S., Swanglap, P., Landes, C. F., & Link, S. (2012). In situ measurement of bovine serum albumin interaction with gold nanospheres. *Langmuir*, 28(24), 9131-9139.
- Du, J., Jin, J., Liu, Y., Li, J., Tokatljan, T., Lu, Z., . . . Lu, Y. (2014). Gold-nanocrystal-enhanced bioluminescent nanocapsules. *ACS Nano*, 8(10), 9964-9969. doi:10.1021/nn504371h
- Ernst, O. P., Sanchez Murcia, P. A., Daldrop, P., Tsunoda, S. P., Kateriya, S., & Hegemann, P. (2008). Photoactivation of channelrhodopsin. *J Biol Chem*, 283(3), 1637-1643. doi:10.1074/jbc.M708039200
- Fischer, H. C., & Chan, W. C. (2007). Nanotoxicity: the growing need for in vivo study. *Current opinion in biotechnology*, 18(6), 565-571.
- Goerke, A. R., Loening, A. M., Gambhir, S. S., & Swartz, J. R. (2008). Cell-free metabolic engineering promotes high-level production of bioactive Gaussia princeps luciferase. *Metab Eng*, 10(3-4), 187-200. doi:10.1016/j.ymben.2008.04.001
- Grabarek, Z. (2006). Structural basis for diversity of the EF-hand calcium-binding proteins. *Journal of molecular biology*, 359(3), 509-525.
- Griesbeck, O., Baird, G. S., Campbell, R. E., Zacharias, D. A., & Tsien, R. Y. (2001). Reducing the environmental sensitivity of yellow fluorescent protein mechanism and applications. *Journal of Biological Chemistry*, 276(31), 29188-29194.
- Gryniewicz, G., Poenie, M., & Tsien, R. Y. (1985). A new generation of Ca²⁺ indicators with greatly improved fluorescence properties. *Journal of Biological Chemistry*, 260(6), 3440-3450.
- Hainfeld, J. F., Liu, W., Halsey, C. M., Freimuth, P., & Powell, R. D. (1999). Ni-NTA-gold clusters target His-tagged proteins. *J Struct Biol*, 127(2), 185-198. doi:10.1006/jsbi.1999.4149
- He, Y. Q., Liu, S. P., Kong, L., & Liu, Z. F. (2005). A study on the sizes and concentrations of gold nanoparticles by spectra of absorption, resonance Rayleigh scattering and resonance non-linear scattering. *Spectrochim Acta A Mol Biomol Spectrosc*, 61(13-14), 2861-2866. doi:10.1016/j.saa.2004.10.035
- Hilge, M., Aelen, J., Perrakis, A., & Vuister, G. W. (2007). Structural basis for Ca²⁺ regulation in the Na⁺/Ca²⁺ exchanger. *Annals of the New York Academy of Sciences*, 1099(1), 7-15.
- Huang, R., Carney, R. P., Ikuma, K., Stellacci, F., & Lau, B. L. (2014). Effects of surface compositional and structural heterogeneity on nanoparticle-protein interactions: different protein configurations. *ACS Nano*, 8(6), 5402-5412.
- Jain, P. K., Lee, K. S., El-Sayed, I. H., & El-Sayed, M. A. (2006). Calculated absorption and scattering properties of gold nanoparticles of different size, shape, and composition: applications in biological imaging and biomedicine. *J Phys Chem B*, 110(14), 7238-7248. doi:10.1021/jp057170o
- Karolin, J. O., & Geddes, C. D. (2012). Reduced lifetimes are directly correlated with excitation irradiance in metal-enhanced fluorescence (MEF). *Journal of fluorescence*, 22(6), 1659-1662.

- Lacerda, S. H. D. P., Park, J. J., Meuse, C., Pristinski, D., Becker, M. L., Karim, A., & Douglas, J. F. (2009). Interaction of gold nanoparticles with common human blood proteins. *ACS Nano*, 4(1), 365-379.
- Larsson, D., Larsson, B., Lundgren, T., & Sundell, K. (1999). The Effect of pH and Temperature on the Dissociation Constant for Fura-2 and Their Effects on $[Ca^{2+}]_i$ in Enterocytes from a Poikilothermic Animal, Atlantic Cod (*Gadus morhua*). *Analytical Biochemistry*, 273(1), 60-65. doi:https://doi.org/10.1006/abio.1999.4210
- Lattanzio, F. A. (1990). The effects of pH and temperature on fluorescent calcium indicators as determined with Chelex-100 and EDTA buffer systems. *Biochemical and Biophysical Research Communications*, 171(1), 102-108. doi:https://doi.org/10.1016/0006-291X(90)91362-V
- Li, Y., & Camacho, P. (2004). Ca^{2+} -dependent redox modulation of SERCA 2b by ERp57. *The Journal of cell biology*, 164(1), 35-46.
- Lindman, S., Lynch, I., Thulin, E., Nilsson, H., Dawson, K. A., & Linse, S. (2007). Systematic investigation of the thermodynamics of HSA adsorption to N-isopropylacrylamide/N-tert-butylacrylamide copolymer nanoparticles. Effects of particle size and hydrophobicity. *Nano letters*, 7(4), 914-920.
- Link, S., & El-Sayed, M. A. (1999). Size and Temperature Dependence of the Plasmon Absorption of Colloidal Gold Nanoparticles. *The Journal of Physical Chemistry B*, 103(21), 4212-4217. doi:10.1021/jp984796o
- Lipp, P., Lüscher, C., & Niggli, E. (1996). Photolysis of caged compounds characterized by ratiometric confocal microscopy: a new approach to homogeneously control and measure the calcium concentration in cardiac myocytes. *Cell Calcium*, 19(3), 255-266. doi:https://doi.org/10.1016/S0143-4160(96)90026-3
- Lipp, P., & Niggli, E. (1993). Ratiometric confocal Ca^{2+} -measurements with visible wavelength indicators in isolated cardiac myocytes. *Cell Calcium*, 14(5), 359-372.
- Liu, Z., Chen, O., Wall, J. B. J., Zheng, M., Zhou, Y., Wang, L., . . . Liu, J. (2017). Systematic comparison of 2A peptides for cloning multi-genes in a polycistronic vector. *Sci Rep*, 7(1), 2193. doi:10.1038/s41598-017-02460-2
- Liz-Marzan, L. M. (2006). Tailoring surface plasmons through the morphology and assembly of metal nanoparticles. *Langmuir*, 22(1), 32-41. doi:10.1021/la0513353
- Mank, M., & Griesbeck, O. (2008). Genetically encoded calcium indicators. *Chem Rev*, 108(5), 1550-1564. doi:10.1021/cr078213v
- Mank, M., Santos, A. F., Drenth, S., Mersic-Flogel, T. D., Hofer, S. B., Stein, V., . . . Borst, A. (2008). A genetically encoded calcium indicator for chronic in vivo two-photon imaging. *Nature methods*, 5(9), 805-811.
- Martin-Garcia, E., Burokas, A., Kostrzewa, E., Gieryk, A., Korostynski, M., Ziolkowska, B., . . . Maldonado, R. (2011). New operant model of reinstatement of food-seeking behavior in mice. *Psychopharmacology (Berl)*, 215(1), 49-70. doi:10.1007/s00213-010-2110-6
- Mie, G. (1908). Beiträge zur Optik trüber Medien, speziell kolloidaler Metallösungen. *Annalen der physik*, 330(3), 377-445.
- Milani, S., Baldelli Bombelli, F., Pitek, A. S., Dawson, K. A., & Rädler, J. (2012). Reversible versus irreversible binding of transferrin to polystyrene nanoparticles: soft and hard corona. *ACS Nano*, 6(3), 2532-2541.

- Miller, M. M., & Lazarides, A. A. (2005). Sensitivity of metal nanoparticle surface plasmon resonance to the dielectric environment. *J Phys Chem B*, 109(46), 21556-21565. doi:10.1021/jp054227y
- Miyawaki, A., Griesbeck, O., Heim, R., & Tsien, R. Y. (1999). Dynamic and quantitative Ca²⁺ measurements using improved cameleons. *Proceedings of the National Academy of Sciences*, 96(5), 2135-2140.
- Miyawaki, A., Llopis, J., Heim, R., McCaffery, J. M., Adams, J. A., Ikura, M., & Tsien, R. Y. (1997). Fluorescent indicators for Ca²⁺ based on green fluorescent proteins and calmodulin. *Nature*, 388(6645), 882-887.
- Moldoveanu, T., Jia, Z., & Davies, P. L. (2004). Calpain activation by cooperative Ca²⁺ binding at two non-EF-hand sites. *Journal of Biological Chemistry*, 279(7), 6106-6114.
- Montenegro, J. M., Grazu, V., Sukhanova, A., Agarwal, S., de la Fuente, J. M., Nabiev, I., . . . Parak, W. J. (2013). Controlled antibody/(bio-) conjugation of inorganic nanoparticles for targeted delivery. *Adv Drug Deliv Rev*, 65(5), 677-688. doi:10.1016/j.addr.2012.12.003
- Muller, M., Bamann, C., Bamberg, E., & Kuhlbrandt, W. (2011). Projection structure of channelrhodopsin-2 at 6 Å resolution by electron crystallography. *J Mol Biol*, 414(1), 86-95. doi:10.1016/j.jmb.2011.09.049
- Nagai, T., Ibata, K., Park, E. S., Kubota, M., Mikoshiba, K., & Miyawaki, A. (2002). A variant of yellow fluorescent protein with fast and efficient maturation for cell-biological applications. *Nature biotechnology*, 20(1), 87-90.
- Nagai, T., Yamada, S., Tominaga, T., Ichikawa, M., & Miyawaki, A. (2004). Expanded dynamic range of fluorescent indicators for Ca²⁺ by circularly permuted yellow fluorescent proteins. *Proceedings of the National Academy of Sciences of the United States of America*, 101(29), 10554-10559.
- Nicotera, P., & Rossi, A. D. (1994). Nuclear Ca²⁺: physiological regulation and role in apoptosis. *Molecular and cellular biochemistry*, 135(1), 89-98.
- Oliver, A. E., Baker, G. A., Fugate, R. D., Tablin, F., & Crowe, J. H. (2000). Effects of temperature on calcium-sensitive fluorescent probes. *Biophysical Journal*, 78(4), 2116-2126.
- Palmer, A. E., & Tsien, R. Y. (2006). Measuring calcium signaling using genetically targetable fluorescent indicators. *Nature protocols*, 1(3), 1057-1065.
- Paredes, R. M., Etzler, J. C., Watts, L. T., Zheng, W., & Lechleiter, J. D. (2008). Chemical calcium indicators. *Methods*, 46(3), 143-151. doi:10.1016/j.ymeth.2008.09.025
- Petr, M. J., & Wurster, R. D. (1997). Determination of in situ dissociation constant for Fura-2 and quantitation of background fluorescence in astrocyte cell line U373-MG. *Cell Calcium*, 21(3), 233-240.
- Raeymaekers, L. (1998). Modelling of some potential effects of luminal Ca²⁺ binding on the kinetics of Ca²⁺ release from the endoplasmic reticulum. *Cell Calcium*, 23(4), 261-268. doi:https://doi.org/10.1016/S0143-4160(98)90124-5
- Rahman, M., Laurent, S., Tawil, N., Yahia, L. H., & Mahmoudi, M. (2013). Nanoparticle and protein corona. In *Protein-nanoparticle interactions* (pp. 21-44): Springer.
- Rehberg, M., Lepier, A., Solchenberger, B., Osten, P., & Blum, R. (2008). A new non-disruptive strategy to target calcium indicator dyes to the endoplasmic reticulum. *Cell Calcium*, 44(4), 386-399.
- Remington, S. J. (2006). Fluorescent proteins: maturation, photochemistry and photophysics. *Current opinion in structural biology*, 16(6), 714-721.

- Rizo, J., & Südhof, T. C. (1998). C2-domains, structure and function of a universal Ca²⁺-binding domain. *Journal of Biological Chemistry*, 273(26), 15879-15882.
- Schäffler, M., Semmler-Behnke, M., Sarioglu, H., Takenaka, S., Wenk, A., Schleh, C., . . . Kreyling, W. G. (2013). Serum protein identification and quantification of the corona of 5, 15 and 80 nm gold nanoparticles. *Nanotechnology*, 24(26), 265103.
- Sparta, D. R., Stamatakis, A. M., Phillips, J. L., Hovelson, N., van Zessen, R., & Stuber, G. D. (2011). Construction of implantable optical fibers for long-term optogenetic manipulation of neural circuits. *Nat Protoc*, 7(1), 12-23. doi:10.1038/nprot.2011.413
- Tannous, B. A., Kim, D.-E., Fernandez, J. L., Weissleder, R., & Breakefield, X. O. (2005). Codon-optimized Gaussia luciferase cDNA for mammalian gene expression in culture and in vivo. *Molecular Therapy*, 11(3), 435-443.
- Tavanti, F., Pedone, A., & Menziani, M. C. (2015). A closer look into the ubiquitin corona on gold nanoparticles by computational studies. *New Journal of Chemistry*, 39(4), 2474-2482.
- Tian, L., Hires, S. A., Mao, T., Huber, D., Chiappe, M. E., Chalasani, S. H., . . . Schreiter, E. R. (2009). Imaging neural activity in worms, flies and mice with improved GCaMP calcium indicators. *Nature methods*, 6(12), 875-881.
- Truong, K., Sawano, A., Mizuno, H., Hama, H., Tong, K. I., Mal, T. K., . . . Ikura, M. (2001). FRET-based in vivo Ca²⁺ imaging by a new calmodulin-GFP fusion molecule. *Nat Struct Biol*, 8(12), 1069-1073. doi:10.1038/nsb728
- Tsai, D.-H., Elzey, S., DelRio, F. W., Keene, A. M., Tyner, K. M., Clogston, J. D., . . . Hackley, V. A. (2012). Tumor necrosis factor interaction with gold nanoparticles. *Nanoscale*, 4(10), 3208-3217.
- Walkey, C. D., Olsen, J. B., Guo, H., Emili, A., & Chan, W. C. (2012). Nanoparticle size and surface chemistry determine serum protein adsorption and macrophage uptake. *Journal of the American Chemical Society*, 134(4), 2139-2147.
- Wang, L., Li, J., Pan, J., Jiang, X., Ji, Y., Li, Y., . . . Chen, C. (2013). Revealing the binding structure of the protein corona on gold nanorods using synchrotron radiation-based techniques: understanding the reduced damage in cell membranes. *J Am Chem Soc*, 135(46), 17359-17368. doi:10.1021/ja406924v
- Wang, P., Wang, X., Wang, L., Hou, X., Liu, W., & Chen, C. (2015). Interaction of gold nanoparticles with proteins and cells. *Sci Technol Adv Mater*, 16(3), 034610. doi:10.1088/1468-6996/16/3/034610
- Welsh, J. P., Patel, K. G., Manthiram, K., & Swartz, J. R. (2009). Multiply mutated Gaussia luciferases provide prolonged and intense bioluminescence. *Biochem Biophys Res Commun*, 389(4), 563-568. doi:10.1016/j.bbrc.2009.09.006
- Willems, K. A., & Van Duyne, R. P. (2007). Localized surface plasmon resonance spectroscopy and sensing. *Annu Rev Phys Chem*, 58, 267-297. doi:10.1146/annurev.physchem.58.032806.104607
- Woodruff, M. L., Sampath, A., Matthews, H. R., Krasnoperova, N., Lem, J., & Fain, G. L. (2002). Measurement of cytoplasmic calcium concentration in the rods of wild-type and transducin knock-out mice. *The Journal of physiology*, 542(3), 843-854.
- Zhan, Q., Zhang, X., Zhao, Y., Liu, J., & He, S. (2015). Tens of thousands-fold upconversion luminescence enhancement induced by a single gold nanorod. *Laser & Photonics Reviews*, 9(5), 479-487. doi:10.1002/lpor.201500013

Zhang, J., Tung, J., Gross, R., & Berglund, K. ((In preparation)). Improved trafficking and expression of luminopsins for more efficient optical and pharmacological control of neuronal activity (In preparation).